

Department of Precision and Microsystems Engineering

Time-of-flight measurements of single-layer tissue with a chip-based optical frequency comb

Nan Li

Report no : 2023.060.

Coach : Dr. Nandini Bhattacharya, Binbin Zhang

Professor : Dr. Nandini Bhattacharya

Specialisation : Optics for Technology (OPT)

Type of report : Master Thesis

Date : 29 August 2023

A microscopic view of a green chip-based optical frequency comb device. A small, rectangular, blue-tinted tissue sample is mounted on the chip. The device features a series of parallel gold-colored lines and a central rectangular area with a grid-like pattern. The background is dark, highlighting the device and the sample.

# Time-of-flight measurements of single-layer tissue with a chip-based optical frequency comb

An Experimental Investigation with chip-based optical frequency combs

MSc Thesis

Nan Li (5627729)

Time-of-flight  
measurements of  
single-layer tissue with a  
chip-based optical  
frequency comb  
**An Experimental Investigation with chip-based  
optical frequency combs**

by

Nan Li (5627729)

Supervisors: (TU Delft) B.Zhang  
(TU Delft) Dr. N . Bhattacharya  
Institution: Delft University of Technology  
Place: the Netherlands  
Project Duration: Sep. 2022 - Aug. 2023

# Abstract

*Cerebral oxygen saturation is an important indicator that reflects the oxygen metabolism of the brain tissues in such patients. The utilization of near-infrared spectroscopy (NIRS) enables the identification of the oxygen saturation levels in nearby tissues by analyzing the distinct oxygenation states of hemoglobin-oxyhemoglobin (HbO<sub>2</sub>) and the distinctive molecular spectrum of deoxygenated hemoglobin (Hb). It is helpful to realize the objective of noninvasive continuous detection on cerebral oxygen saturation because near-infrared radiation can directly penetrate the skull to obtain the characteristics of the average oxygen saturation of the brain tissues. This also allows a noninvasive way to monitor blood flow in the brain. A frequency comb is a pulsed laser in the time domain and a sequence of discrete, uniformly spaced frequency lines in the frequency domain. Applying the frequency comb to NIRS has the potential to develop a high-speed and fs-level time-of-flight resolution blood flow measurement system. The objective of this thesis is to utilize a chip-based optical frequency comb as an illuminating source in order to conduct time-of-flight measurements of a single target, employing a Michelson interference experiment. The establishment of the time of flight in the single-layer case and the investigation of the non-ambiguity range form the fundamental basis for future experiments multi-layer.*

# Acknowledgments

Time is cracking on, I will graduate from Delft University of Technology soon, and goodbye to this beautiful city. I would like to express my heartfelt gratitude to all the people who have supported and guided me through the project.

First and foremost, I feel sincerely grateful to my supervisor Dr.Nandini Bhattacharya and Binbin Zhang. Both for their enlightening advice and instructions without preservation during the whole process of the whole research. With prudence and patience, they point the way to my thesis improvement so I can finish this project better. I also want to express thanks to the Electronics technician Bradley But and Ir. Joel Hazan from TU/e. Without the help of them, it is not possible to build the experiment setup.

Last but not least, my cordial thanks to my family and friends whose unconditional support always encourages me in my whole master project.

*Nan Li*

*Aug. 20, 2023*

*Delft, the Netherlands*

# Contents

<b>Abstract</b>	<b>i</b>
<b>Acknowledgments</b>	<b>ii</b>
<b>1 Introduction</b>	<b>1</b>
<b>2 Theory</b>	<b>4</b>
2.1 Diffuse Optics . . . . .	4
2.2 Near-infrared spectroscopy (NIRS) . . . . .	5
2.2.1 Continuous Wave Near-Infrared Spectroscopy (CW-NIRS) . . . . .	6
2.2.2 Frequency Domain Near-Infrared Spectroscopy (FD-NIRS). . . . .	7
2.2.3 Time Domain Near-Infrared Spectroscopy (TD-NIRS) . . . . .	7
2.3 Optical frequency comb (OFC) . . . . .	10
2.3.1 Mode-Locked laser . . . . .	11
2.3.2 Integrated optical frequency comb . . . . .	13
<b>3 Experiment</b>	<b>15</b>
3.1 Mode-locked(ML) semiconductor laser . . . . .	15
3.1.1 Chip Laser . . . . .	15
3.1.2 Laser Diode Drive Circuit (PCB) . . . . .	19
3.2 Theoretical Background. . . . .	20
3.3 Setup . . . . .	23
3.4 Measurement . . . . .	24
<b>4 Results and Discussions</b>	<b>26</b>
4.1 Experiment Result . . . . .	26

- 4.2 Interference spectral pattern analysis . . . . . 27
  - 4.2.1 Peak Interval Method . . . . . 27
  - 4.2.2 Non-ambiguity range . . . . . 31
- 4.3 Discussion . . . . . 34
- 5 Conclusion and Outlook 37**
  - 5.1 Conclusion . . . . . 37
  - 5.2 Outlook . . . . . 38
- References 42**

# 1

## Introduction

A crucial measure of brain health is cerebral blood flow (CBF). CBF impairment is a direct cause of dangerous clinical conditions such as ischemic stroke since CBF fluctuates extensively over time and the brain is at significant risk for injury from inappropriately low or high perfusion with diminishing cerebral autoregulatory capacity[1]. Moreover, cerebral oxygen saturation is an important indicator that reflects oxygen metabolism. Changes in cerebral perfusion can be observed by monitoring regional cerebral oxygen saturation ( $rSO_2$ ). The change of  $rSO_2$  is related to the change of cerebral blood flow when cerebral metabolism, circulating blood volume, arterial blood oxygen content, blood flow transit time, and fractional oxygen extraction are held constant. Therefore, the change of cerebral blood flow in the frontal lobe can be indirectly understood through the frontal  $rSO_2$  [2]. Many techniques for monitoring the brain have been developed in both academic and clinical contexts. Transcranial Doppler (TCD) ultrasound uses the sound wave to examine brain activity. Electroencephalography (EEG) captures the electrical activity created by neuronal firing, while magnetoencephalography (MEG) records the magnetic field generated by cerebral activity[3][4]. Functional Magnetic Resonance Imaging (fMRI) is a functional neuroimaging procedure measuring brain activity by detecting changes in blood flow associated with neural activity[5]. Considering mobility,

---

risk, and both temporal and spatial resolution, a portable, noninvasive, all-in-one, high spatial and temporal resolution technique is preferable [6]. The exponentially expanding discipline of diffuse optics affords us the opportunity to meet many of these requirements.

Near-infrared spectroscopy (NIRS) uses near-infrared light to measure the optical properties of a medium, absorption, and scattering. Given those optical properties, we can detect oxygen saturation of local tissues based on the different oxygenations of the hemoglobin-oxyhemoglobin ( $HbO_2$ ) and the differentiated molecular spectrum of deoxygenated hemoglobin ( $Hb$ ). In addition, it is advantageous to achieve the goal of noninvasive continuous detection on cerebral oxygen saturation since near-infrared radiation may be used to directly enter the skull and measure the average oxygen saturation of the brain tissues [7]. The optical frequency comb is a femtosecond pulsed light source that exhibits a consistent temporal interval in the time domain and is characterized by a sequence of discrete and evenly spaced spectral lines in the optical domain, which can provide excellent frequency accuracy and high spectral purity, as well as broad spectral coverage [8]. Recently, the utilization of semiconductor laser platforms has been the subject of research with regard to their potential as sources of OFC, for instance, mode-locked integrated external-cavity surface-emitting lasers (MIXSELS). Moreover, the integrated chip-based frequency combs have been demonstrated in several platforms, which come up with the benefits mentioned above and excellent wearability features simultaneously [9]. However, applying OFC to measuring diffusing medium is not fully explored, especially the optical properties.

The objective of this project is to employ an optical frequency comb that is generated by a mode-locked chip laser as a source of light for conducting time-of-flight (distance) measurements on a single target. These measurements will be carried out utilizing the principle of Michelson interference studies. The determination of a single layer will serve as the fundamental basis for further measurements pertaining to the optical characteristics of tissues composed of multi-layer. Furthermore, this study aims to explore the methodologies for quantifying temporal delay, examining the correlation between temporal (spatial) resolution and bandwidth, and identifying the parameter that determines the non-ambiguity range.

This report starts with background information about near-infrared spectroscopy (NIRS) and optical frequency comb(OFC), including chip-based laser. Chapter 3 of this report encompasses a comprehensive presentation of the experimental design. This includes a detailed account of the introduction and testing of the equipment, an exposition of the theoretical foundation of the experiment, and a thorough description of experimental procedures. In Chapter 4, an account is provided of the processing of the experimental results and the subsequent analysis conducted on the processed data. Chapter 5 provides a comprehensive summary of the entire experiment, while also offering an overview of future studies.

# 2

## Theory

This chapter will explain the theory behind near-infrared spectroscopy (NIRS) and optical frequency comb(OFC), including chip-based laser. The following sections will provide a deeper understanding of the characteristics of each technology.

### 2.1 Diffuse Optics

As introduced in the previous section 1, to study biological tissues (e.g., monitor CBF), the field of diffuse optics provides the chance to understand the photon propagation in a highly scattering medium and meet the criteria. Before we begin the more detailed discussion of NIRS and OFC, we briefly introduce diffuse optics. Most theoretical formulations of diffuse optics begin with transport theory. The key factor of the formulations is the light radiance,  $L(r, \hat{\Omega}, t)$  defined as the light power per unit area traveling in the  $\hat{\Omega}$  direction at position  $r$  and time  $t$ . And  $L(r, \hat{\Omega}, t)$  is determined by the radiation transport equation (RTE)

$$\frac{1}{v} \frac{\partial L(r, \hat{\Omega}, t)}{\partial t} + \hat{\Omega} \cdot \nabla L(r, \hat{\Omega}, t) = -\mu_t L(r, \hat{\Omega}, t) + Q(r, \hat{\Omega}, t) + \mu_s \int_{4\pi} L(r, \hat{\Omega}', t) f(\hat{\Omega}, \hat{\Omega}') d\hat{\Omega}' \quad (2.1)$$

where  $f(\hat{\Omega}, \hat{\Omega}')$  is a normalized differential cross-section for single light scattering events in the medium and it provides the probability that dispersed light will be scattered in the direction  $\hat{\Omega}'$ , assuming that its incident direction was  $\hat{\Omega}$ .  $Q(r, \hat{\Omega}, t)$  is the power per volume by sources at position  $r$  and the time  $t$  in the  $\hat{\Omega}$  direction. Coefficient  $\mu_t = \mu_a + \mu_s$  illustrates the loss of light from each infinitesimal volume element relies on the absorption and scattering coefficient in the volume. In addition,  $\mu_s$  is the light scattering coefficient,  $\mu_a$  is the light absorption coefficient, and  $v$  is the speed of light in the medium. After using  $P_N$  approximation and applying the assumption that normalized differential scattering cross-section  $f$  depends only on the angle between the incident and outgoing scattering wavevectors, the photon diffusion equation for the photon fluence rate is obtained [1] [10].

$$\nabla \cdot (D(r) \nabla \Phi(r, t)) - v\mu_a(r)\Phi(r, t) - \frac{\partial \Phi(r, t)}{\partial t} = -vS(r, t) \quad (2.2)$$

where the photon diffusion coefficient  $D(r) \equiv \frac{v}{3(\mu'_s(r) + \mu_a(r))}$ , and  $\mu'_s$  is reduced scattering coefficient ( $\mu'_s = \frac{1}{\ell_{tr}}$ ),  $\ell_{tr}$  is transport mean-free path.

## 2.2 Near-infrared spectroscopy (NIRS)

Near-infrared spectroscopy (NIRS) theoretically provides a technique for continuous, noninvasive, bedside cerebral blood flow (CBF) monitoring. In 1977, Jobsis demonstrated the ability of near-infrared spectroscopy to detect changes in adult cortical oxygenation during hyperventilation [11]. With the NIRS method, a short light signal is delivered to the tissue, and after propagation, the emitted signal, which carries information on tissue constituents, is measured. Figure 2.1 illustrates the typical measurement of the brain using NIRS. The proper physical models for photon migration (e.g., diffusion, random walk, Monte Carlo) are used to interpret the difference between the incident and detected light signal [12].

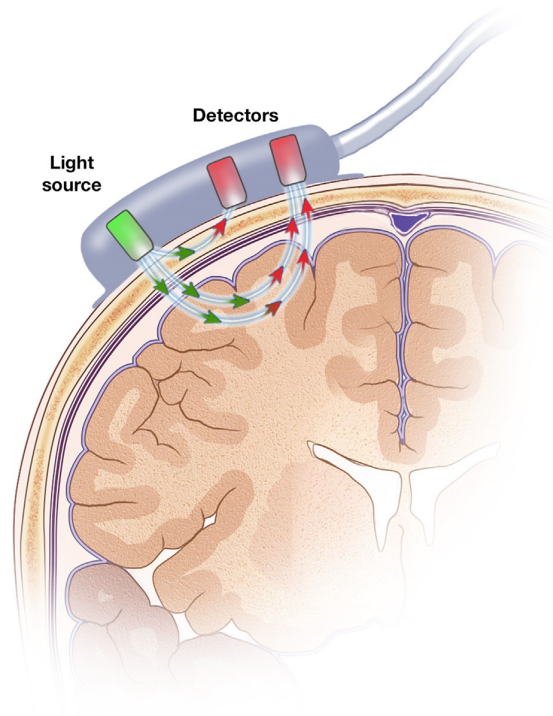


Figure 2.1: Measurement of the brain using NIRS[13]

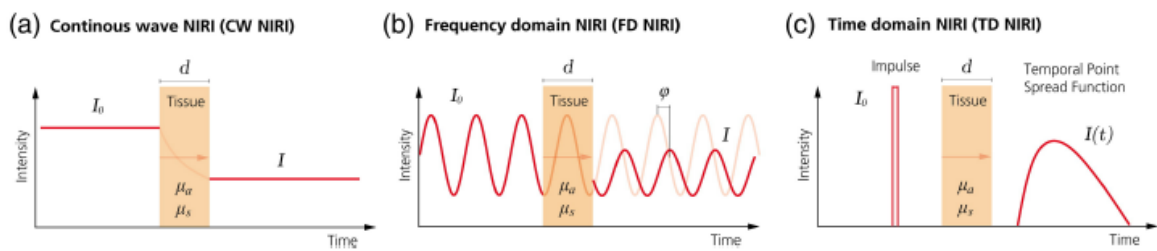


Figure 2.2: Comparison of the three variants of NIRS, illustrating the type of light used to probe the tissue[7]

Generally, NIRS is typically classified into three types based on the type of incident light used and what the detector measures, which are continuous wave NIRS (CW-NIRS), frequency domain NIRS (FD-NIRS), and time domain NIRS (TD-NIRS). Figure 2.2 illustrates these types.

### 2.2.1 Continuous Wave Near-Infrared Spectroscopy (CW-NIRS)

The CW-NIRS technique is the most straightforward among the three methods and is also cost-effective to execute as it requires only basic instrumentation. As shown in figure 2.2, CW-NIRS systems use a constant-amplitude continuous light to illuminate the tissue and look at the changes in intensity. The issue at hand pertains to the lack of

knowledge regarding the trajectory of photons. Consequently, this constraint restricts the scope of measurement to alterations in concentration exclusively, precluding the determination of absolute values [14].

### 2.2.2 Frequency Domain Near-Infrared Spectroscopy (FD-NIRS)

FD-NIRS is a more advanced form of NIRS that involves the modulation of the intensity of the source and the simultaneous measurement of both intensity changes and phase. The standard or conventional geometry is as follows in figure 2.1. The experimental procedure involves the injection of intensity-modulated light into the source, followed by the measurement of phase shift and intensity changes as a function of source sector separation using photon-counting detectors. Then the proportional relationship between the phase shift and the propagation distance allows for direct measurement of the Differential path length factor (DPF). Moreover, by utilizing analytical solutions for the propagation of light within the tissue, it is possible to make estimations regarding the optical characteristics of the medium. However, the limitation persists: the time-of-flight resolution is not yet fully achieved [7].

### 2.2.3 Time Domain Near-Infrared Spectroscopy (TD-NIRS)

The most advanced form of NIRS is TD-NIRS, which uses short pulses on the order of a few picoseconds. The experimental procedure entails injecting this short pulse into tissue and measuring photons' temporal broadening or temporal point spread function as they traverse the tissue via time-of-flight analysis. The aforementioned curve can be fitted using diffusion theory in order to derive accurate quantitative optical characteristics, thereby facilitating the quantification of saturation [12]. As mentioned in the previous paragraph, a short pulse laser is employed instead of a light source that continually illuminates the tissue. As a result of its scattering and absorption properties, the photons then disperse through the tissue, with some never reaching the detector. Accordingly, the light pulse is delayed, broadened, and attenuated after exiting the tissue. Based on the emitted pulses, optical properties may be determined. TD-NIRS systems measure the TOF of individual photons. After recording the TOF of a sufficient number of

photons into a histogram, the temporal point spread function (TPSF) can be generated. In other words, the TPSF is called the distribution of time-of-flight (DTOF).

The most common method for measuring the TPSF is called time-correlated single photon counting (TCSPC). In TCSPC practice, the temporal profile of the NIRS signal is obtained by periodically measuring the delay between the injected laser pulse and the photon's arrival. After a sufficient number of photons, the histogram illustrates the shape of the TPSF. A photon with a time-of-flight that corresponds to the TPSF peak is far more likely to reach the detector than one with a time-of-flight that corresponds to the far end of the tail due to the important fact that there are always more photons when the intensity is higher. Figure 2.3 shows the concept of time-correlated single photon counting.

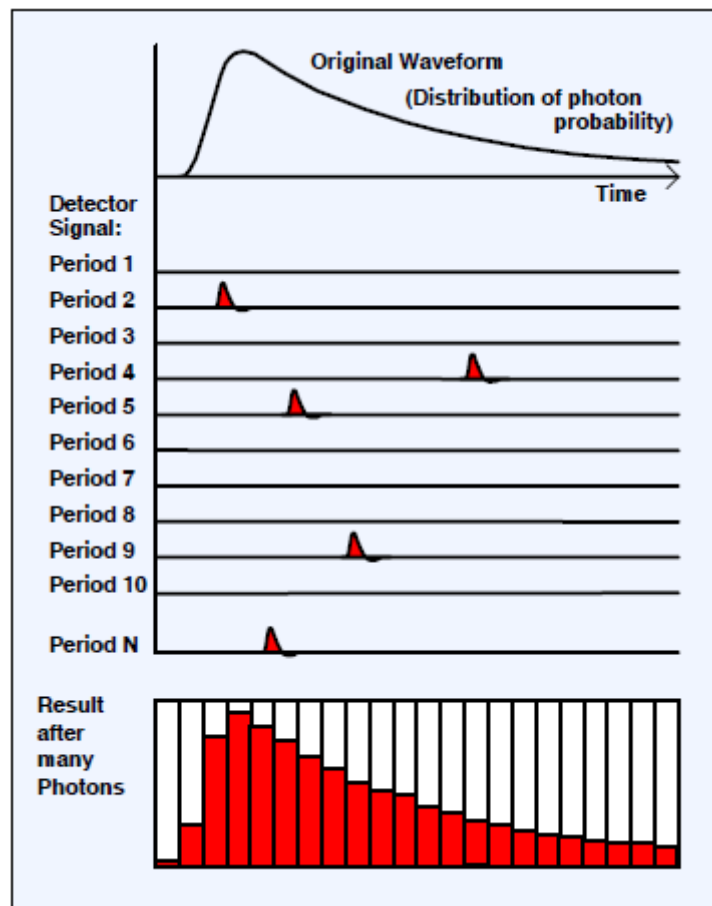
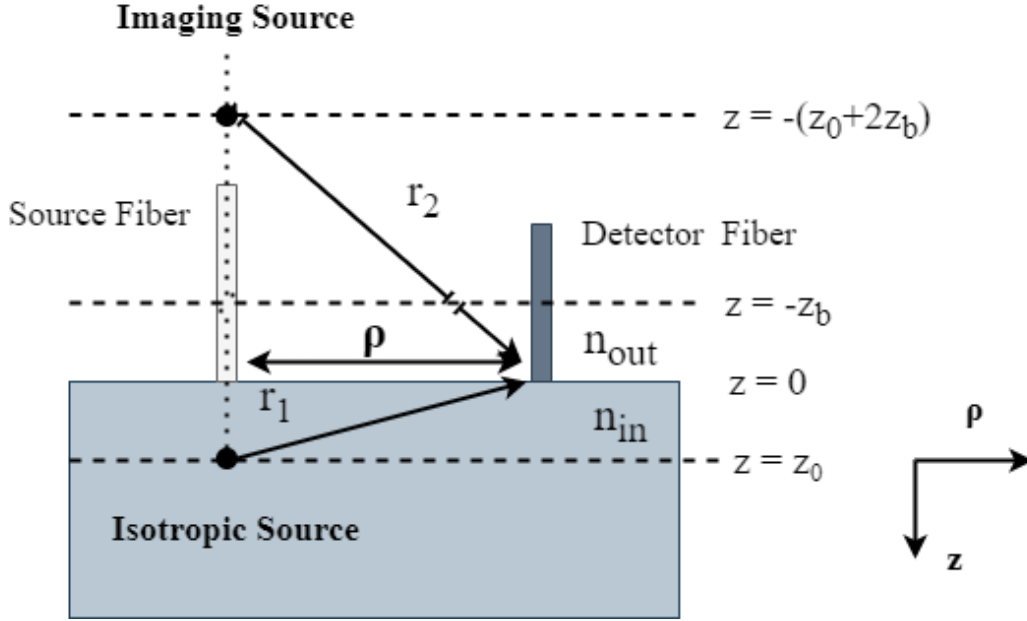


Figure 2.3: Concept of time-correlated single photon counting [7]

The preceding paragraph demonstrates the methodology employed to measure TPSF. In addition, section 2.1 illustrates the diffusion equation, which was first proposed by

Patterson et al. in 1989 [7] [15]. Based on that, optical properties are used to develop the theoretical model of light transport for a light pulse. The semi-infinite geometry and the extrapolated-zero boundary condition are employed in this study since they are commonly used for models of approximate tissue. Equation (2.3) and figure 2.4 illustrate the case.



**Figure 2.4:** Semi-infinite geometry with extrapolated boundary condition

$$\Phi(z = -z_b) = 0 \quad (2.3)$$

where  $z_b$  illustrates a zero-crossing point for the fluence rate at a distance  $z_b$ , outside of the tissue, and  $R_{eff}$  is the effective reflection coefficient and depends on the relative refractive index.

$$z_b = 2 \cdot \ell_{tr} \frac{1 + R_{eff}}{3(1 - R_{eff})} = \frac{2}{3\mu'_s} \frac{1 + R_{eff}}{3(1 - R_{eff})} \quad (2.4)$$

Then, utilizing Green's function (frequency domain)(equation 2.5)in semi-infinite geometry with an extrapolated-zero boundary condition (equation 2.3), the theoretical TPSF can be determined in equation(2.9).

$$G_0([\rho, z], [\rho_s = 0, z_s = \ell_{tr}]) = \frac{1}{4\pi} \left[ \frac{\exp(-kr_1)}{r_1} - \frac{\exp(-kr_2)}{r_2} \right] \quad (2.5)$$

where

$$k \equiv \sqrt{(\mu_a v - i\omega)/D} \quad (2.6)$$

$$r_1 = \sqrt{(z - \ell_{tr})^2 + \rho^2} \quad (2.7)$$

$$r_2 = \sqrt{(z + 2z_b + \ell_{tr})^2 + \rho^2} \quad (2.8)$$

And in equation (2.6),  $\omega$  is the laser or source modulation frequency.

$$\Phi_{TD}(t) = \frac{vS}{(4\pi Dt)^{3/2}} \left[ \exp\left(-\frac{r_1^2}{4Dt}\right) - \exp\left(-\frac{r_2^2}{4Dt}\right) \right] \exp(-v\mu_a t) \quad (2.9)$$

The equation (2.9) enables us to predict the light intensity as a function of time.

After observing the TPSF, an algorithm can be employed to tune the relevant parameters,  $\mu_a$  and  $\mu'_s$ , until the measurement and theory are in optimum agreement. Moreover, the amplitude of the histogram is dependent on the measurement time. Therefore, it must be normalized for fitting. Obviously, this presupposes that the conditions used in the theoretical derivation correspond to the conditions used in the measurement. The semi-infinite geometry with the extrapolated-zero border condition is utilized in this case. This means that while doing the measurement, the tissue volume must be sufficient to neglect the effects of the distant margins. In addition, the photon propagation through the medium can be described as a diffusion process, which is  $\mu'_s \gg \mu_a$ .

## 2.3 Optical frequency comb (OFC)

As mentioned before, time-correlated single photon counting (TCSPC) is employed in TD-NIRS, and the photons are detected sequentially. However, it leads to low temporal resolution and a long collection time. Besides, detecting only one photon at a time will cause the experiment to be affected by ambient light. TD-NIRS employs a laser with a pulse duration of a few tens of picoseconds and optical frequency combs can achieve a pulse duration of femtosecond [12] [16]. Optical frequency combs can attain time resolutions in the picosecond range, whereas TD-NIRS employs light sources that offer time resolutions of up to nanoseconds [17]. Therefore, utilization of an optical frequency comb has the potential to enhance temporal resolution comparison to TD-NIRS.

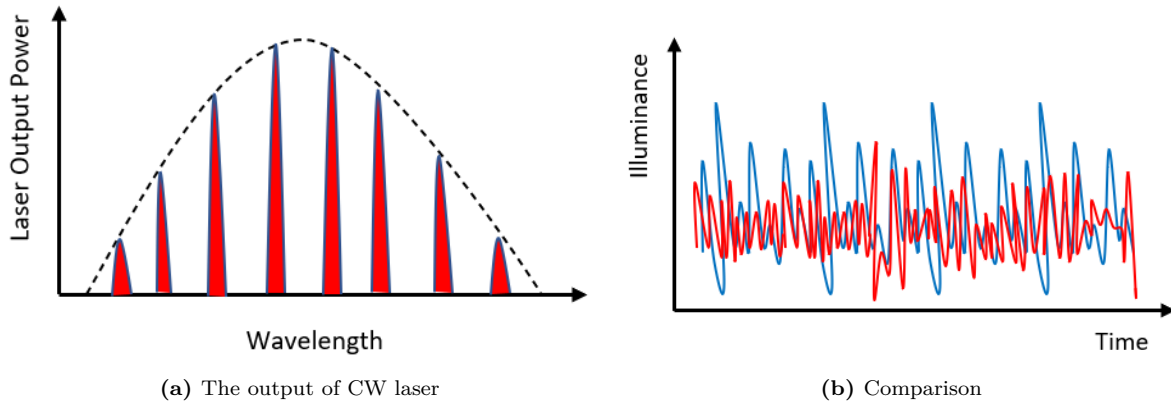


**Figure 2.5:** (a) The output of CW laser (b) Comparison of the beat signal (on leaving the cavity) when all the modes are in phase (in blue) and with random phases between the modes (in red)

### 2.3.1 Mode-Locked laser

Prior to discussing the optical frequency comb, it is imperative to grasp the concept of mode-locking, as it serves as the predominant method for generating an optical frequency comb using a mode-locked laser. Typically, a laser possesses an inherent bandwidth that is intricately linked to both the gain medium and the optical cavity. Within the cavity, the incident light waves will engage in constructive and destructive interference, forming stationary waves. The resonant cavity permits the longitudinal modes, which refer to the unique sets of frequencies of a standing wave, to oscillate and vibrate autonomously. The output of a laser, known as a continuous wave (cw), is composed of numerous modes, numbering in the thousands, as depicted in figure 2.5a. The laser emits a significant number of frequencies, resulting in a complex beat signal, as depicted by the red line in Figure 2.5b. In order to achieve a consistent waveform for the beat signal, it is imperative to synchronize the phase of the constituent waves. This is because the shape of the beat signal is contingent upon the relative phase of waves possessing distinct frequencies. A coherent beat-frequency signal is generated when all the waves radiated by a cavity are in phase. In the cavity, specific temporal and spatial locations exist where the waves synchronize in phase, resulting in a highly potent interference signal. This phenomenon is depicted by the blue line in figure 2.5b.

As shown in figure 2.5b, all of the modes of a cw laser are fixed in phase, and the lasers will periodically interfere with each other. Consequently, the laser generates a light pulse train and is referred to as mode-locked. By setting the relative phases of all

the lasing longitudinal modes, mode-locked lasers create ultrashort, repeating optical pulse trains. The associated spectrum can be written as  $f_n = n f_{\text{rep}} + f_0$ , where  $n$  is a large integer,  $f_{\text{rep}}$  is the repetition frequency of the envelope of the pulses, and  $f_0$  is the carrier-envelope offset frequency, related to the phase shift  $\Delta\phi$  by the relationship  $f_0 = f_{\text{rep}} \Delta\phi / 2\pi$ . With the previous phase lock, the repetition frequency  $f_{\text{rep}}$  is controlled with a cw laser. However, the offset frequency  $f_0$  can still shift. In order to address this issue, it is necessary to measure and regulate  $f_0$  through the utilization of a method known as self-referencing, shown in figure 2.6. There is a comb that spans an octave and takes the red side of the spectrum. Utilizing a nonlinear optical material for the purpose of frequency doubling, specifically targeting light within the blue region of the electromagnetic spectrum, results in the formation of interference that directly yields the offset frequency. The mode-locked laser operates by manipulating the repetition rate frequency to establish a fixed rate at which the pulses are emitted. Additionally, the offset frequency is utilized to regulate the deviation of the carrier relative to the phase  $\Delta\phi_{CEO}$  during each occurrence, which is shown in figure 2.7.

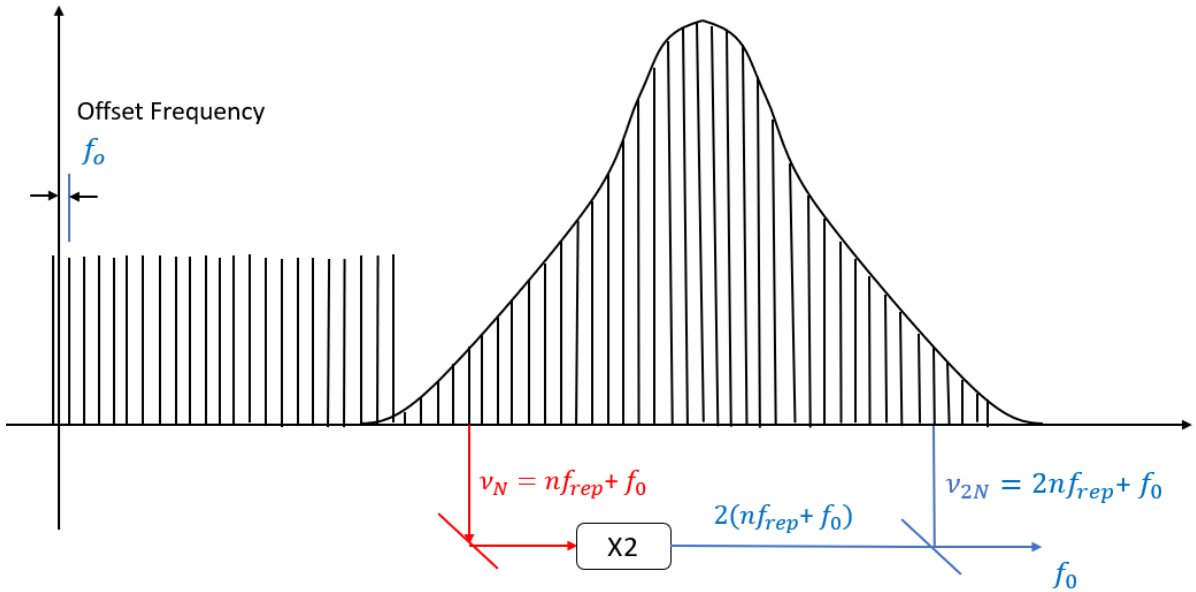


**Figure 2.6:** Offset frequency detection via self-referencing

After accurately measuring and precisely controlling the repetition rate ( $f_{\text{rep}}$ ) and the offset frequency ( $f_0$ ), it is possible to synchronize them with an atomic clock. Then the spectrum that the repetition rate of the laser separates each pulse train can be obtained, and the spectral lines are called an optical frequency comb (OFC). Figure 3.2

shows the optical frequency comb in the time and frequency domain.

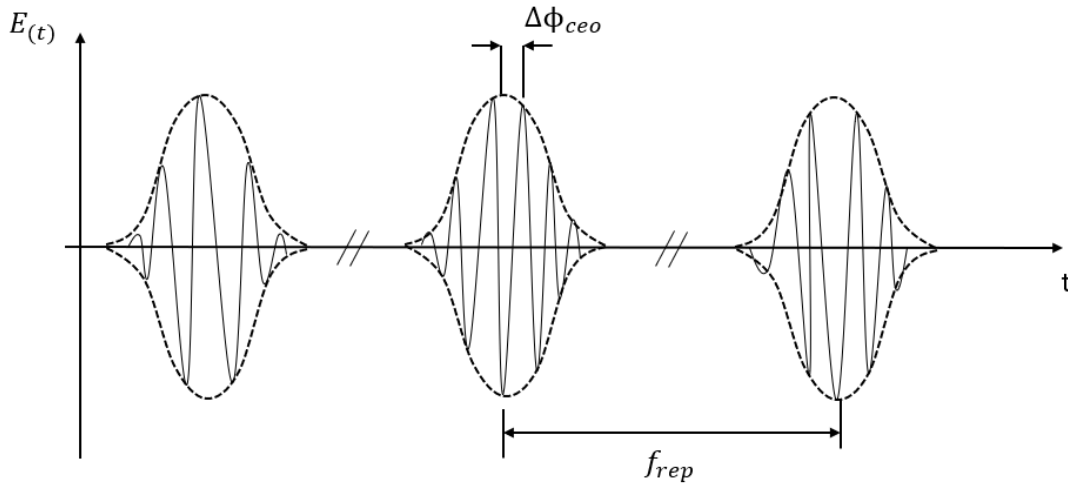


**Figure 2.7:** Frequency domain of an optical frequency comb

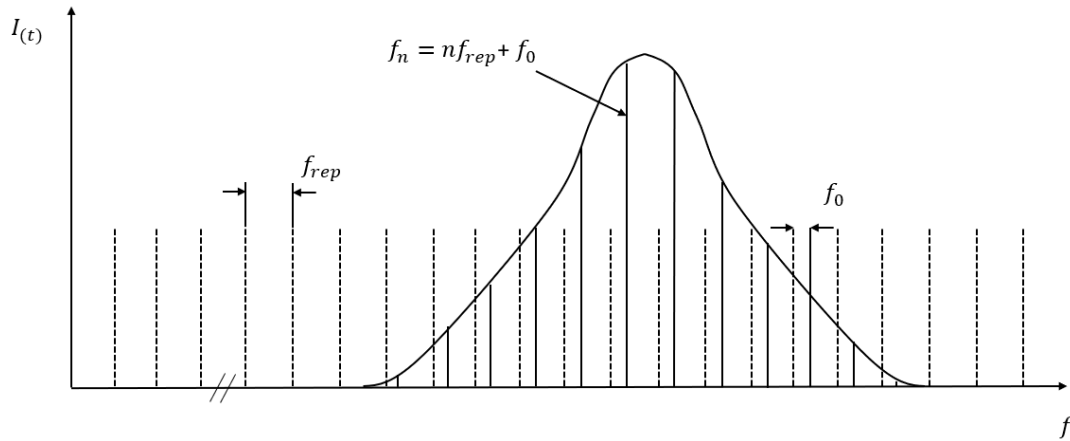


**Figure 2.8:** Time domain of an optical frequency comb

### 2.3.2 Integrated optical frequency comb

In the preceding section, the Optical Frequency Comb (OFC) was introduced as a technology that provides unparalleled precision in frequency measurement. Despite their evident value and significance, technologies based on optical frequency combs (OFCs) were predominantly utilized in research laboratories due to their reliance on cumbersome, energy-intensive, and costly equipment for generating, controlling, and manipulating comb light. In the last twenty years, there has been significant progress in the field of integrated photonics, specifically in the development of silicon-based integrated

---

photonics. This advancement has facilitated the manufacturing of optical fiber communication (OFC) devices by employing sophisticated lithography and nanofabrication methods. By utilizing contemporary manufacturing infrastructure, integrated photonics significantly reduces system size, weight, power consumption, and cost[18]. Thus, it offers a cost-effective, energy-efficient solution that fulfills the preferences mentioned in Chapter 1.

# 3

## Experiment

This chapter will present a comprehensive overview of the experimental setup employed in this research.

### 3.1 Mode-locked(ML) semiconductor laser

#### 3.1.1 Chip Laser

As mentioned in 2.3.2, mode-locked (ML) semiconductor lasers, when implemented as photonic integrated circuits (PIC), are particularly well-suited for the development of compact devices used in distance metrology sensing [19], high-resolution optical spectroscopy [20], high-precision frequency clocks [21], and optical communication systems [22]. In order to function as a comb generator, a mode-locked (ML) laser must primarily possess a wide output comb and maintain a consistent frequency spacing between the optical modes of the frequency comb.

Moreover, Mode locking is a technique to generate ultrashort pulses from a laser. There are two main types of mode locking: active and passive. The technique of active mode locking involves the utilization of an external modulator to periodically alter either

the loss or the phase of the laser cavity. This process facilitates the synchronization of the laser modes, resulting in the formation of a pulse. Passive mode locking employs a saturable absorber, which exhibits a decrease in absorption with exposure to high-intensity light, to adjust the loss within the laser cavity. Passive mode locking can generate significantly shorter pulses compared to active mode locking due to the faster response of the saturable absorber to shorter pulse durations. Passive mode-locking exhibits enhanced durability, simplicity, and compactness while enabling the emission of shorter pulses than lasers operated by active mechanisms [23]. Hence, passive mode locking is presently the predominant approach employed for achieving mode locking, and we will employ a passively mode-locked laser in our experimental setup.

In this study, the utilization of a quantum well based InP Passively Mode-Locked laser operating at a wavelength of 1300 nm is employed in order to attain laser linewidths of reduced width, pulse durations on the order of subpicosecond, and optical frequency combs with broad spectral coverage, while the repetition frequency of the optical frequency comb was 20.4 GHz. The integrated InP quantum well (QW) based multi-longitudinal mode (ML) laser, as depicted in figure 3.1, was manufactured by Joel Hazan from Eindhoven University of Technology. The operation of the device involves applying forward bias to the longer gain section, which functions as a semiconductor optical amplifier (SOA), and reverse bias to the shorter section, which serves as a saturable absorber (SA). Figure 3.2a presents an optical microscope image of the laser, highlighting the significant components, namely the semiconductor optical amplifier (SOA) and the saturable absorber (SA). In this laser design, the absorber section spans a length of  $100\mu m$ , while an electrical isolation section measuring  $20\mu m$  is situated between the SOA and the SA.

Moreover, it is imperative to investigate the correlation between the characteristics of light intensity and laser dynamics with respect to the current of the semiconductor optical amplifier (SOA) and the reverse bias voltage of the saturable absorber (SA) to attain the intended light intensity. In this case, the Laser Diode Controller Modules for the PRO8000 platform (manufactured by THORLABS) are employed as the current source, while the Bench Power Supply EL302RT (produced by AIM-TTI INSTRUMENTS) is utilized as the voltage source. This configuration is depicted in figure 3.3. Figure 3.4

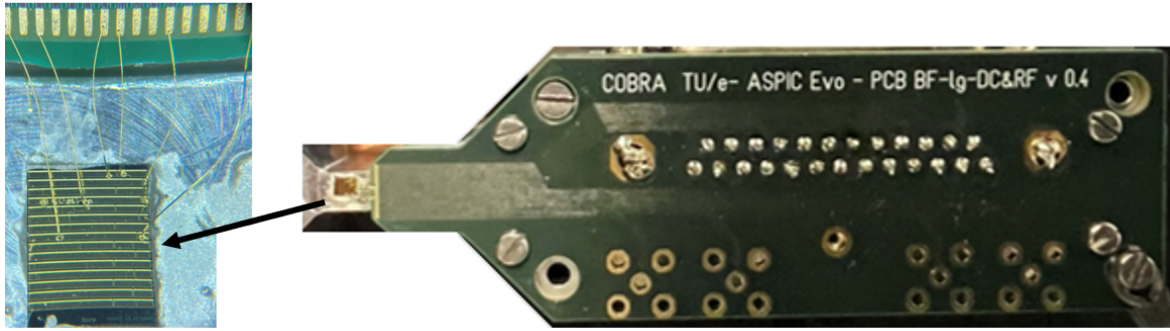


**Figure 3.1:** Top view of the chip laser

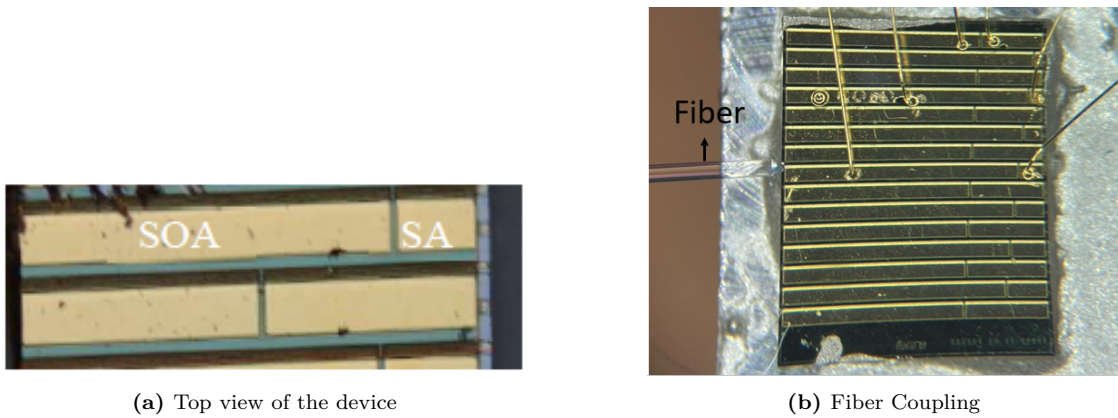


**Figure 3.2:** (a) Top view of the Device Under Test with the SA and SOA sections and (b) Laser Coupling

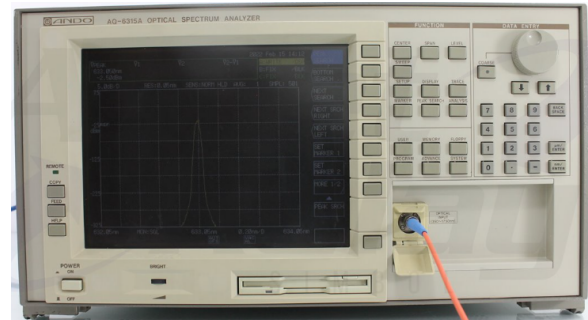
illustrates the schematic representation of the experiment setup employed for the characterization of the 2mm laser. In the experimental setup, a single-mode tapered and lensed fiber is employed to gather the output of the two-section laser. The process of coupling is depicted in Figure 3.2b. In addition, an optical isolator is integrated into the system to mitigate the ingress of back-reflected light into the laser, which can adversely affect its overall operational efficiency. Furthermore, a water cooling mechanism is employed to regulate the temperature of the chip platform, maintaining it at approximately 18 degrees Celsius. The laser output was examined using a lightwave multimeter (HP 8153A). According to the thesis from Joel Hazan [23], the threshold current, as determined through calculations, is observed to be 50 mA when a reverse bias voltage of -1 V is applied to the semiconductor amplifier (SA). When a reverse bias voltage of -1 V is applied to the saturable absorber (SA), the threshold current is measured to be 48 mA. In this study, the reverse bias voltage was set to -1 V, while the light intensity was controlled by manipulating the injection current.



(a) Current Source



(b) Voltage Source



(c) Optical spectrum analyzer

**Figure 3.3:** (a) The current source used in this experiment; (b) The voltage source used in this experiment. (c) Optical spectrum analyzer used in this experiment

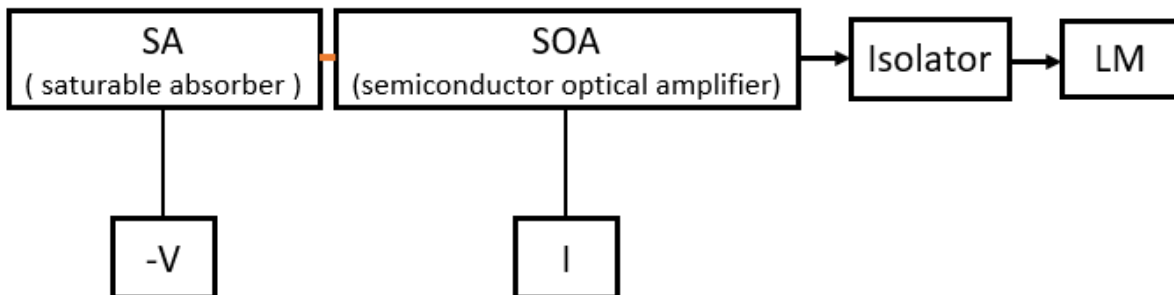


**Figure 3.4:** Experiment Setup used to test the laser

The spectrum of the output laser at a current of 70 mA is depicted in Figure 3.5. The spectrum obtained at a current of 70 mA exhibits a skewed Gaussian-like form, characteristic of a mode-locked semiconductor laser. The optical spectrum analyzer (AQ-6315A) has a maximum resolution of 0.05 nm, which is insufficient for discerning the comb structure. The only mathematical function that is observable to us is the cosine function based on figure 3.5. As mentioned in section 3.1.1, it has been established that the laser generated by the Eindhoven University of Technology exhibits a repetition frequency of 20.4 GHz. figure 3.5 shows that the inter-peak distance  $\Delta\lambda$  measures 0.12

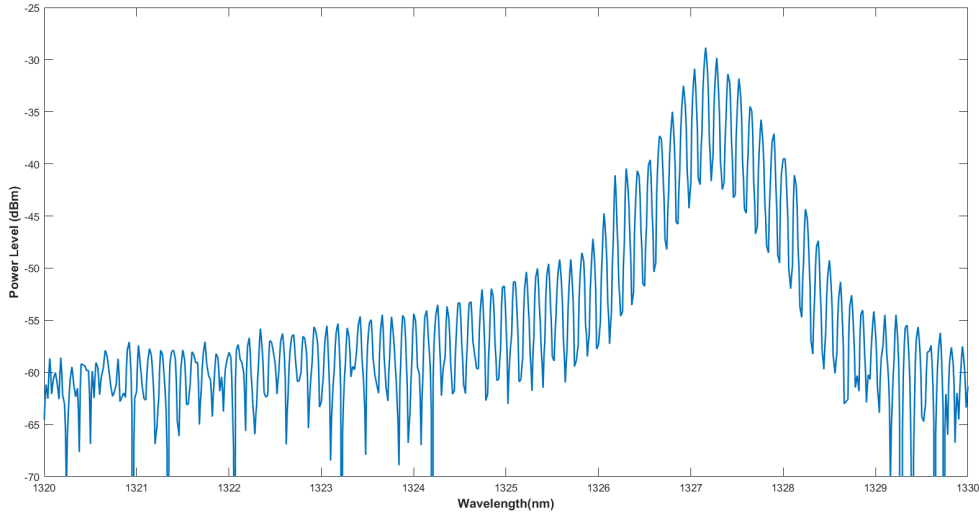


**Figure 3.5:** Spectrum at 0.05nm resolution

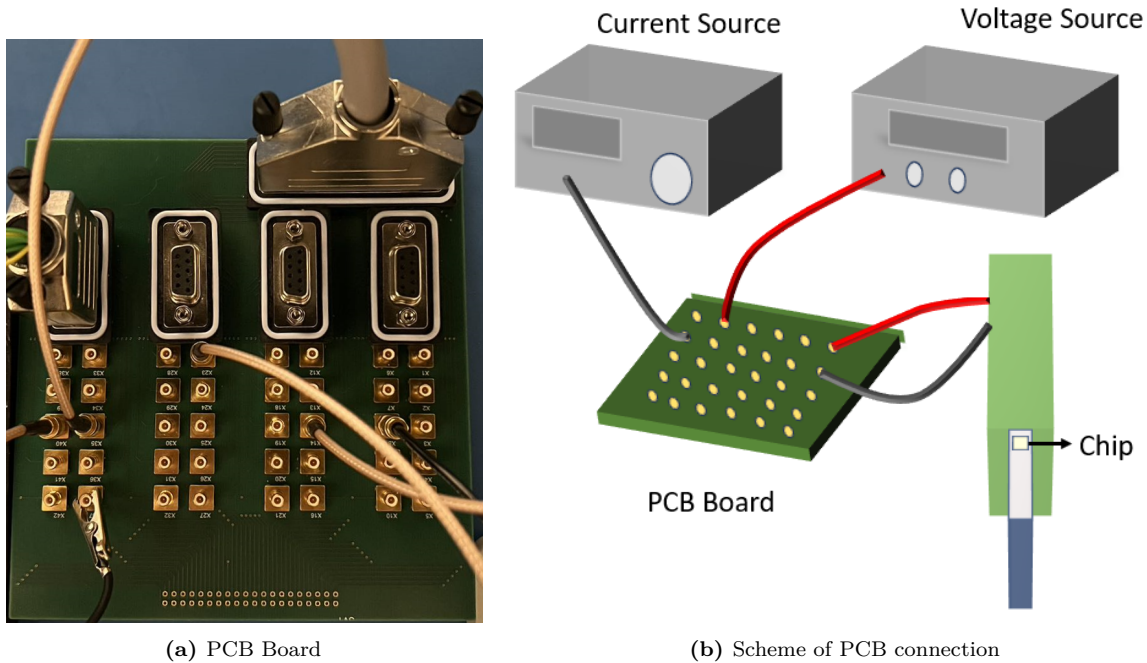
nm, while the central wavelength  $\lambda$  is determined to be 1325 nm, and the wave velocity  $c$  is  $2.9979 \cdot 10^8$  m/s. Using the equation 3.2, it is feasible to ascertain that the repetition frequency of the frequency comb amounts to 20.491 GHz, thereby aligning with the anticipated theoretical value.

$$f = \frac{c}{\lambda} \quad (3.1)$$

$$df = \frac{c}{\lambda^2} * d\lambda \quad (3.2)$$

### 3.1.2 Laser Diode Drive Circuit (PCB)

As stated in section 3.1.1, the activation of a chip laser requires it to be connected to a current and voltage source. In this particular scenario, a printed circuit board (PCB) is utilized to establish a connection between the chip laser and the sources, as depicted in Figure 3.6. The chip laser establishes an electrical connection between the current and voltage sources by utilizing a 25-pin D sub-connector. The current source is linked to the printed circuit board (PCB) through a 9-pin D sub-connector. Furthermore, the black line depicted in figure 3.6 establishes a connection between the chip and the platform to the ground. The PCB board has been designed with assistance from Esteban Venialgo



(a) PCB Board

(b) Scheme of PCB connection

**Figure 3.6:** (a) Printed Circuit Board (b) Scheme of PCB Connection

Araujo and Binbin Zhang. The schematic diagram of the connection is depicted in Figure 3.6b.

## 3.2 Theoretical Background

The feasibility of employing the interferometric methodology to detect diffusing light has been demonstrated. Therefore, the interferometry technique will be employed to ascertain the distance and subsequently obtain the time-of-flight (TOF), thereby generating the time-point spread function (TPSF). Subsequently, it becomes feasible to acquire optical properties. Therefore, a Michelson interferometer is employed to achieve the interferometry. The pulse train released by the comb source is divided into two beams recombining after traveling through a series of optical delays. The spectrum is detected and recorded using a spectrometer.  $L$  represents the difference in length between the reference beam and the measuring beam, which is shown in figure 3.7.

In the following section, we proceed to present the fundamental concept of spectral interferometric ranging. The comb can be expressed as  $E(t)$  in the time domain and  $E(\mu)$  in the frequency domain. The carrier frequency is  $\omega_c$ . The electric field signal of

a femtosecond laser pulse in the time domain can be expressed as:

$$E(t) = \sqrt{I(t)}e^{i\omega_c t + i\phi_0} \quad (3.3)$$

where  $I(t)$  represents the pulse light intensity,  $\phi_0$  is the initial phase. The Fourier transform of the time domain optical pulse signal yields the corresponding representation in the frequency domain, which can be expressed as:

$$E(v) = \text{FT}[E(t)] = \sqrt{S[v]}e^{i\phi(v)} \quad (3.4)$$

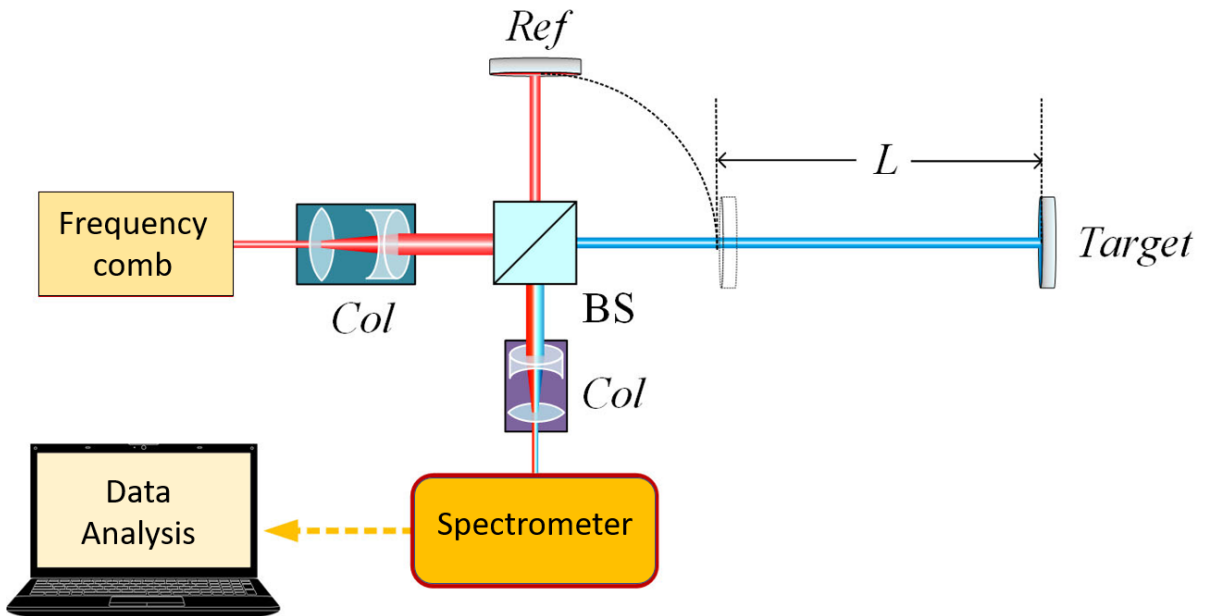


**Figure 3.7:** Schematic of the distance measurement system with Michelson interferometer

where  $S[v]$  represents the power spectrum of the frequency comb,  $\phi(v)$  represents the phase spectrum of each frequency. The structure of the interferometric optical path is shown in figure 3.7: the Michelson interferometric optical path is used as the main part, and the difference in optical range between the measurement and the reference optical path produces a fixed time delay to form an interference in the frequency domain.

The red part is the reference arm, and the blue part is the measurement arm, the difference in length between the two forms the optical range difference  $2L$ , the reference mirror  $Ref$  keeps the same position during the measurement, the measurement mirror

*Target* moves back and forth to change the optical range difference, the pulses from the optical frequency comb are expressed as reference pulses  $E_{ref}(t)$  and measurement pulse  $E_t(t)$  after the beam splitter BS. The time delay of the measurement light relative to the reference light is expressed as  $\tau$ , the pulses are reflected separately and converge on BS when spectral interference occurs in the frequency domain, and the spectrometer records the interference fringes. However, the power of  $E_{ref}(t)$  and  $E_t(t)$  are affected by factors such as the optical coupling efficiency and beam splitting ratio. It is difficult to ensure strict equality, which is expressed as inconsistent electric field signal intensity and can be written as

$$\begin{aligned} E_{ref}(t) &= aE(t) \\ E_t(t) &= bE(t - \tau) \end{aligned} \quad (3.5)$$

where  $a$  and  $b$  are the corresponding power factors, ideally  $a = b = 0.5$ , which are usually not equal in actual experiments due to environmental and other conditions, resulting in the change of the oscillation amplitude of the interferometric signal  $I(t)$ :

$$\begin{aligned} E(t) &= E_{ref}(t) + E_t(t - \tau) \\ E(v) &= \text{FFT}(E(t)) = aE(v) + bE(v)e^{-jw\tau} \\ I(v) &= E^2(v) = (aE(v) + bE(v)e^{-jw\tau}) * (aE^*(v) + bE^*(v)e^{jw\tau}) \\ &= E^2(v) [a^2 + b^2 + 2ab \cos(2\pi\tau v)] \end{aligned} \quad (3.6)$$

As observed in equation 3.6, the interference signal contains two parts, AC term, and DC term, the intensity of the DC term is  $E^2(v)(a^2 + b^2)$ , AC term is  $E^2(v)(2ab \cos(2\pi\tau v))$ . The frequency domain interference signal after Fast Fourier Transform (FFT) results in equation 3.7, there will be two impulse functions of  $\delta(t - \tau)$  and  $\delta(t + \tau)$ , due to the amount of time sought in this coordinate system, and the time domain transformation is relatively even, we call the transformed coordinate system as the pseudo-time domain.

$$\begin{aligned} I(t) &= \text{FFT}[I(v)] \\ I(t) &= I_0(t) \otimes [ab\delta(t - \tau) + (a^2 + b^2) \delta(t) + ab\delta(t + \tau)] \end{aligned} \quad (3.7)$$

The DC component is constant since we only evaluate the dispersive impact. In this case, the DC component is neglected. However, the DC term is larger than the

AC term, which will provide noise. Balanced detection (BD) reduces the DC noise[24]. The AC term of the interfering signal is a cosine function before the transformation. However, in the pseudo-time domain, it is represented as two impulse functions with frequency  $\tau$  and appearing axisymmetrically,  $\Delta t = f_{ac}[I(v)] = \tau$ . The calculation of  $\tau$  can be equated to the measurement of  $L$ , since  $L = \frac{\tau c}{2}$ . Using  $\tau$ , the TOF can be determined. This is for single-layer measurement. For multi-layer measurement(tissue), the different temporal delay  $\tau_1\tau_2\tau_3\tau_4 \cdots \tau_n$  are acquired between the measured light and the reference light for the AC component. Similarly, we can obtain the TOF of each layer and produce the TPSF based on the equation 3.8[25][26]. Then as described in 2.2.3, the optical properties  $\mu_a$  and  $\mu'_s$  can be obtained.

$$\begin{aligned}
E(t) &= E_{ref}(t) + E_t(t - \tau_1) + E_t(t - \tau_2) + E_t(t - \tau_3) + \cdots + E_t(t - \tau_n) \\
E(v) &= \text{FFT}(E(t)) \\
&= aE(v) + b_1E(v)e^{-jw\tau_1} + b_2E(v)e^{-jw\tau_2} + b_3E(v)e^{-jw\tau_3} + \cdots + b_nE(v)e^{-jw\tau_n} \\
I(v) &= E^2(v) \\
&= (aE(v) + b_1E(v)e^{-jw\tau_1} + b_2E(v)e^{-jw\tau_2} + b_3E(v)e^{-jw\tau_3} + \cdots + b_nE(v)e^{-jw\tau_n}) \\
&\quad * (aE^*(v) + b_1E^*(v)e^{jw\tau_1} + b_2E^*(v)e^{jw\tau_2} + b_3E^*(v)e^{jw\tau_3} + \cdots + b_nE^*(v)e^{jw\tau_n}) \\
&= E^2(v)[a^2 + b_1^2 + b_2^2 + \cdots + b_n^2 + 2ab_1 \cos(2\pi\tau_1v) + 2ab_2 \cos(2\pi\tau_2v) + \cdots \\
&\quad + 2ab_n \cos(2\pi\tau_nv) + 2b_1b_2 \cos(2\pi(\tau_1 - \tau_2)v) + \cdots + 2b_{n-1}b_n \cos(2\pi(\tau_{n-1} - \tau_n)v)]
\end{aligned} \tag{3.8}$$

where  $b_1 \cdots b_n$  are very low compare to  $a$ , and  $a^2 \gg a \cdot b_n \gg b_{n-1} \cdot b_n$ , so the terms include  $b_{n-1} \cdot b_n$  can be neglected.

This study aims to examine the properties of a single layer by employing a mirror to reflect laser light as a means to address the constraints imposed by time.

### 3.3 Setup

According to section 3.2, the experiment setup is built based on the Michelson interferometer, and the schematic diagram is shown in figure 3.9a. The real experiment setup, as depicted in figure 3.8, was constructed according to the provided scheme. The reflector used for measurement was mounted onto the electrically controlled one-dimensional

rail, as illustrated in figure 3.9b. The reflector was securely fixed in place.

In the experiment, the comb laser is generated and modulated by the mode-locked laser, the repetition rate of the comb is 20.4 GHz. The isolator can prevent the occurrence of back-reflection. In order to mitigate the impact of laser loss resulting from free space, the fiber optic coupler (90:10) is employed. A collimator is employed for the purpose of light emission measurement due to the Gaussian nature of the emitted light. This characteristic ensures that a significant portion of the energy is concentrated in the central region, facilitating efficient light emission.

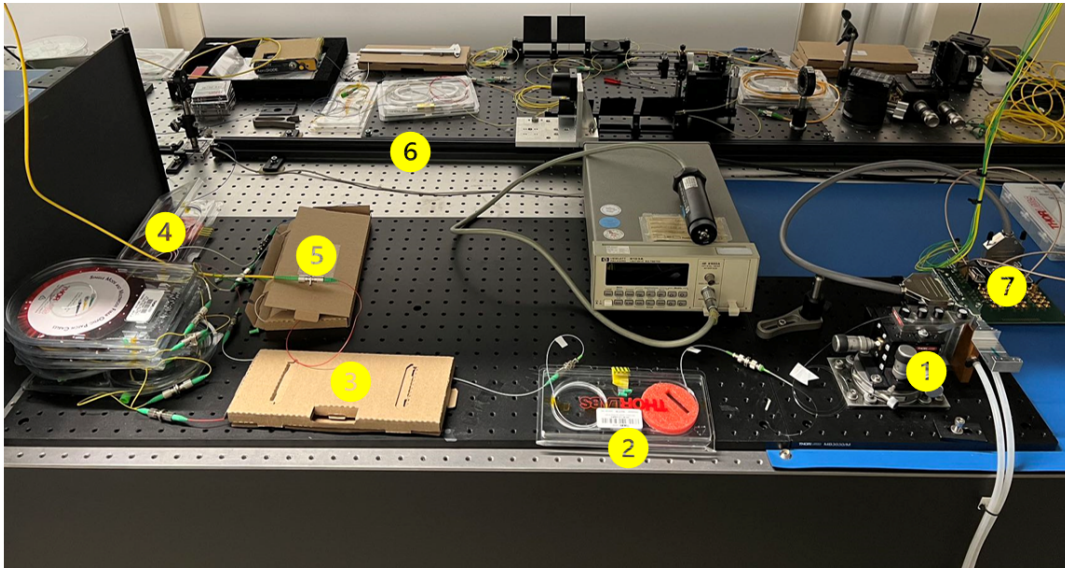


**Figure 3.8:** Top view of experiment setup(1: Chip laser; 2: Isolator; 3: Fiber optic coupler 90:10 ratio; 4: Fiber optic circulator; 5: Fiber optic coupler 50:50 ratio; 6: Rail; 7: PCB board)

### 3.4 Measurement

In this experimental study, we adhere to the prescribed methodology illustrated in figure 3.4 to establish a connection between the fiber and laser in order to attain the anticipated power output of 2 mW. Subsequently, the light source is connected to the optical loop. In order to ascertain the interference pattern on an optical analyzer, one may elect to decrease the resolution to obtain a smooth comb spectrum, in this case, the resolution is set as 0.1nm. Observing the interference signal can be beneficial. Moving the reflector and observing the interference pattern is accomplished by propelling the tram along the rail. In this experimental procedure, the tram is incrementally displaced by 1 mm for

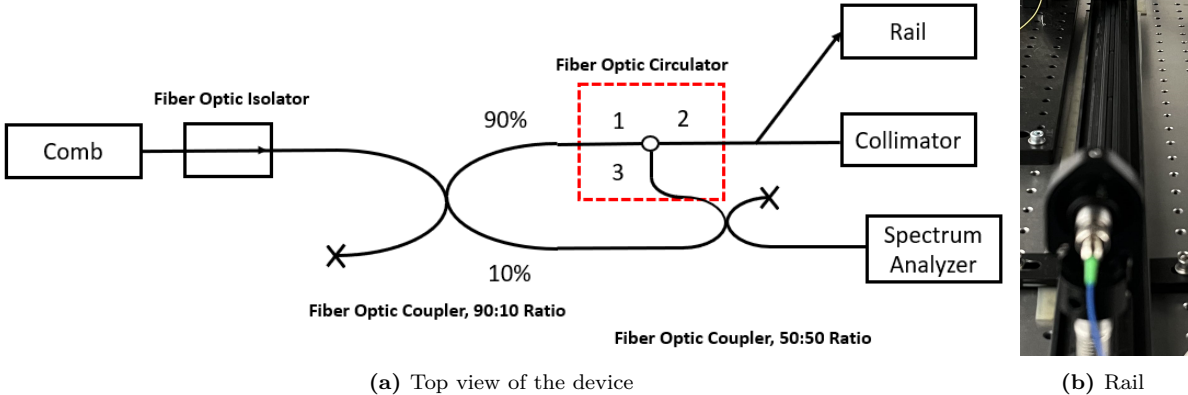


Figure 3.9: (a) Schematic diagram of the experiment setup; (b) Rail

16 iterations while simultaneously capturing the corresponding interference pattern on the spectrometer at each point.

# 4

## Results and Discussions

This chapter aims to provide a detailed review of the experiment's findings and conduct a thorough analysis of the outcomes.

### 4.1 Experiment Result

As mentioned in Chapter 3, the trolley was displaced 16 times with incremental movements of 1 mm in order to capture spectral interference patterns at each position. Figure 4.1 depicts the interference patterns seen at the first, fifth, ninth, and thirteenth displacements. Based on equation 3.7, the Fast Fourier Transform (FFT) applied to the interference spectrum will combine the frequency domain outcomes into the pseudo time domain. This transformation includes the DC term, where the 0 point corresponds to a pulse signal. The transverse coordinates of  $\pm\tau$  will exhibit a symmetrical appearance, resulting in two relative theoretical intensities of the pulse signal for a and b. The peak spacing approach is employed to analyze the Fast Fourier Transform (FFT) output map. This method involves directly identifying the peak position in order to acquire the transverse coordinates of  $\tau$ . The method in question is referred to as the Peak Interval Method.

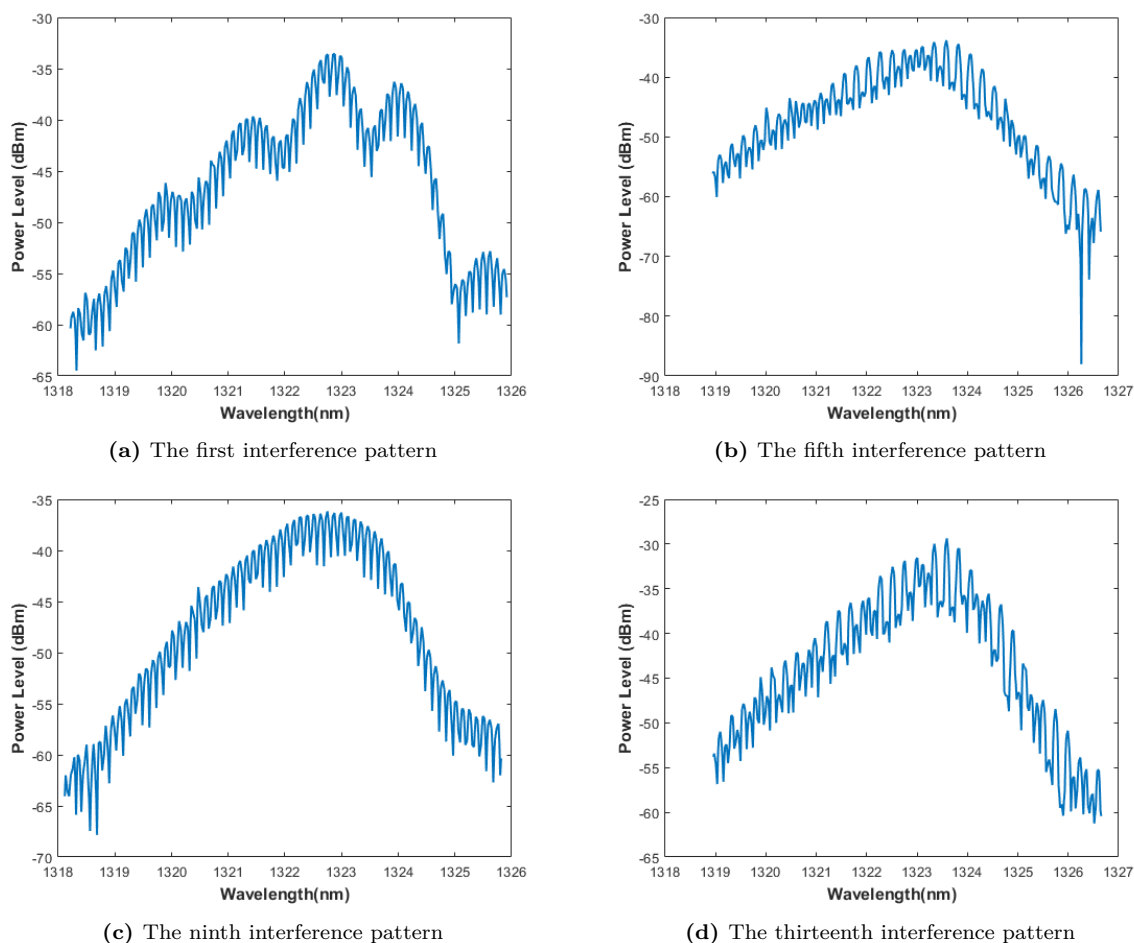


**Figure 4.1:** The spectral interferograms correspond to the orders of magnitude one, five, nine, and thirteen.

## 4.2 Interference spectral pattern analysis

In this experiment, a total of 16 sets of interference patterns were acquired. The last step involves analyzing the obtained results in order to determine the time delay and non-ambiguity distance.

### 4.2.1 Peak Interval Method

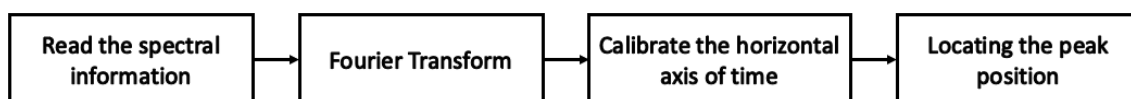


**Figure 4.2:** Peak interval method process

It is sufficient to conduct a single Fast Fourier Transform to obtain the outcomes by employing the peak interval approach. However, it is necessary to calibrate the horizontal axis in order to establish an accurate time axis. Figure 4.2 illustrates the flow of the peak interval approach.

The horizontal axis of the uncalibrated time-axis FFT transform result is  $[-\frac{N}{2}, \frac{N}{2}]$ , where  $N$  is the number of horizontal axis points and is a positive even number, the same as the number of sampled spectral data, in this case,  $N$  is 500. Equation 3.2 provides the repetition frequency, which is subsequently utilized in equation 4.1 to determine the sampling frequency  $f_s$  in the time domain. Equation 4.2, on the other hand, yields the temporal resolution  $d\tau$ , which is 0.78 ps. The temporal cross-axis is obtained by multiplying the temporal resolution by the cross-axis coordinates of the uncalibrated FFT transform.

$$f_s = \frac{1}{df} \quad (4.1)$$

$$d\tau = \frac{f_s}{N} = \frac{1}{df \cdot N} \quad (4.2)$$

Additionally, sampling frequency  $f_s$ , number of horizontal axis points  $N$  and spectral bandwidth  $B$  can be expressed in equation 4.3. The temporal resolution  $\tau$  can be illustrated by equation 4.4. Moreover, the spatial resolution can be obtained by analyzing the temporal resolution, shown in equation 4.5. It is understood that there exists an inverse relationship between spatial resolution and bandwidth, whereby a narrower bandwidth corresponds to a higher spatial resolution.

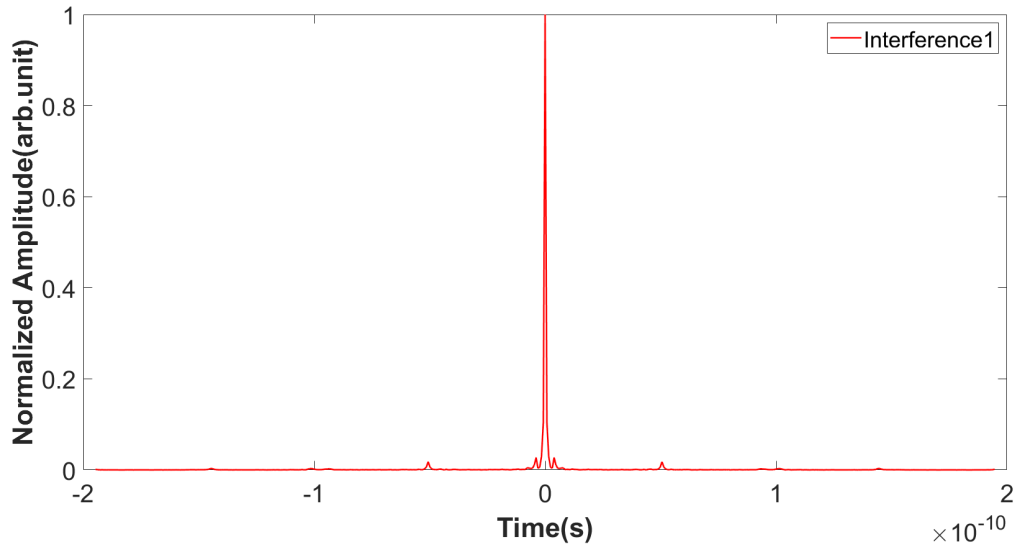
$$f_s = \frac{N}{B} \quad (4.3)$$

$$d\tau = \frac{f_s}{N} = \frac{1}{B} \quad (4.4)$$

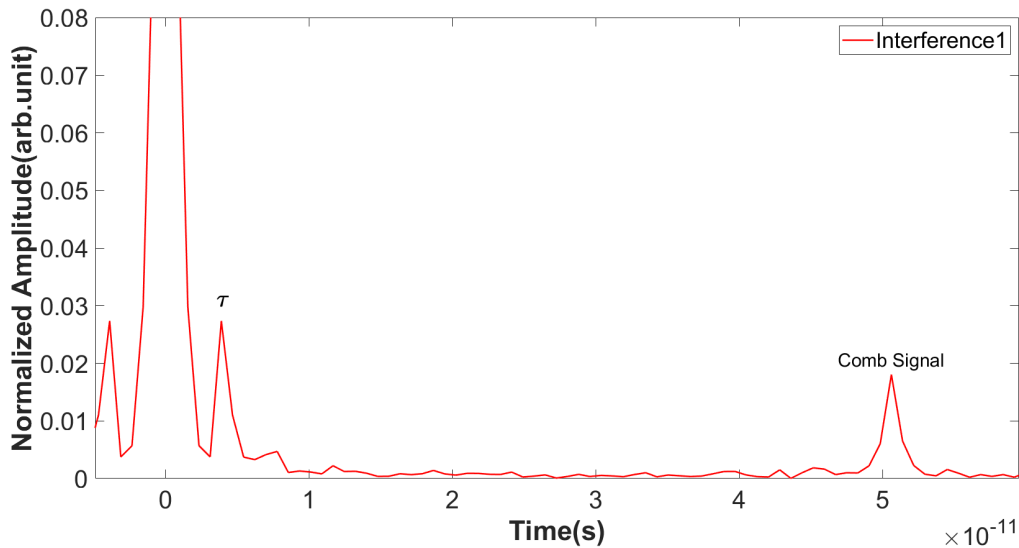
$$d_L = \frac{d\tau \cdot c}{2} = \frac{c}{2 \cdot B} \quad (4.5)$$

Figure 4.3 is derived through the use of Fourier transformation and subsequent calibration of the temporal axis, utilizing the first dataset of interference fringes. Upon further examination of zoom-in figure 4.4, it becomes apparent that the optical frequency comb signal depicted in section 5.1 is indeed there. The aforementioned conclusion is

derived from the observation that the 16 occurrences of the pseudo-time domain image are appropriately positioned within this particular area. Furthermore, the Fourier transform of the time-domain plots for each of the 16 spectral interferograms can be analyzed to ascertain the temporal delays  $\tau$  of the recorded light at various points in relation to the reference light.



**Figure 4.3:** The Fourier Transform result of the first pattern with the calibrated horizontal axis of time



**Figure 4.4:** Zoom in view of the Fourier transform result of spectral interference

The time delay  $\tau$  at each place is determined by localizing the peak position using the peak interval method after getting the Fourier transform results of the interference

spectra at each position. For instance, figure 4.6 illustrates the Fourier transform result for the first interference spectrum, from which one can read that the time delay  $\tau_1$  is 3.89 ps.

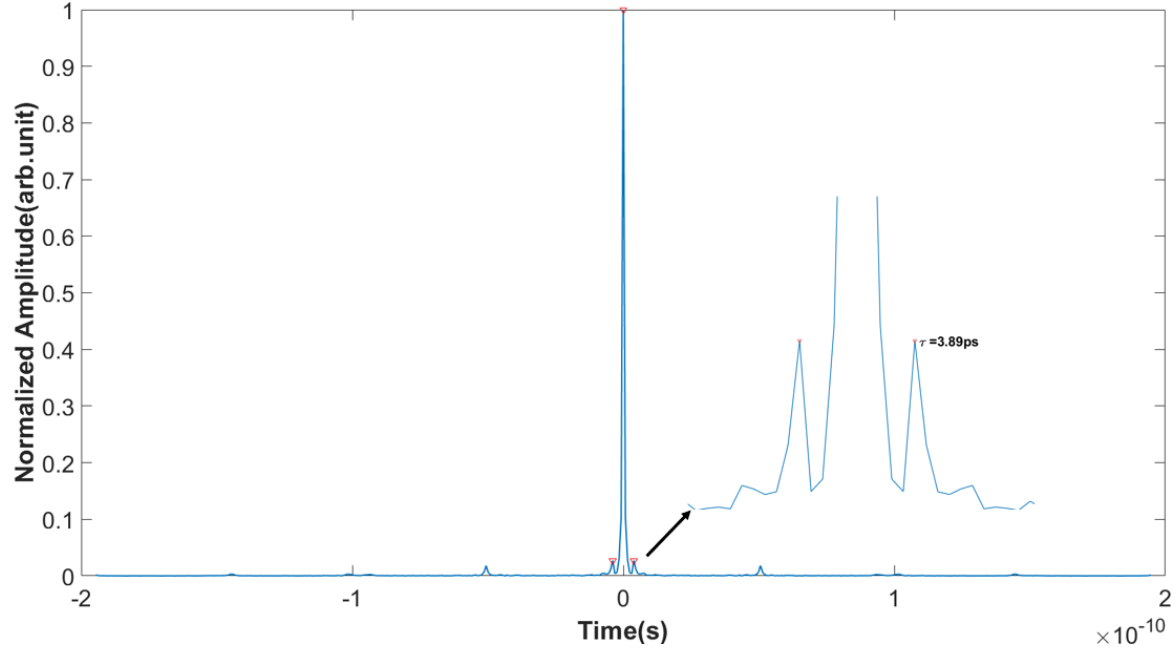


Figure 4.5: Locate the peak position for the first interferometric spectra

Table 4.1 presents the time delays derived from sixteen interferometric spectra following Fourier transformations. Figure 4.6 illustrates the temporal delay corresponding to the table.

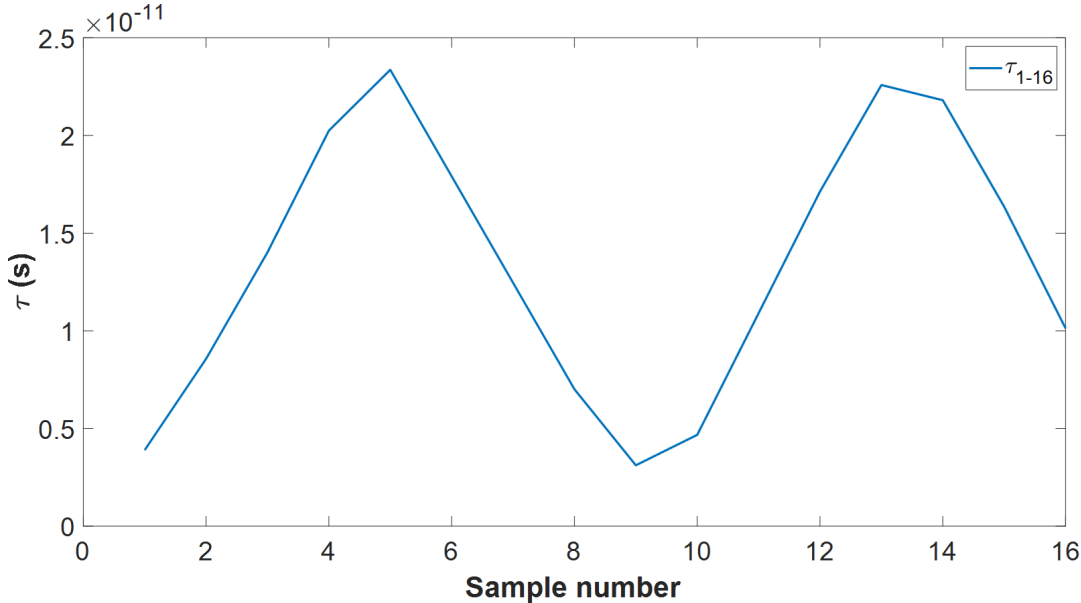


Figure 4.6: Temporal delay

Sample Number	Delay Time (s)
1	$3.8936 \times 10^{-12}$
2	$8.5659 \times 10^{-12}$
3	$1.4017 \times 10^{-11}$
4	$2.0247 \times 10^{-11}$
5	$2.3362 \times 10^{-11}$
6	$1.7911 \times 10^{-11}$
7	$1.2460 \times 10^{-11}$
8	$7.0085 \times 10^{-12}$
9	$3.1149 \times 10^{-12}$
10	$4.6723 \times 10^{-12}$
11	$1.0902 \times 10^{-11}$
12	$1.7132 \times 10^{-11}$
13	$2.2583 \times 10^{-11}$
14	$2.1804 \times 10^{-11}$
15	$1.6353 \times 10^{-11}$
16	$1.0123 \times 10^{-11}$

**Table 4.1:** The delay time for sixteen interference

In this study, we are doing measurements on a singular target (single layer), which is then expanded to encompass a multi-target scenario (multiple layers). This multi-layer analysis allows us to determine the time delays associated with each layer. By consolidating these time delays into a single plot, we are able to generate an image depicting the time of flight for light to traverse the multi-layer structure.

### 4.2.2 Non-ambiguity range

Based on the information provided in the preceding section, it is established that the time delay  $\tau$  derived from the Fourier-transformed interference spectrum can be obtained through the utilization of the peak spacing approach. In this section, the Non-ambiguity range will be investigated. Moreover, this case will exclusively focus on the Non-ambiguity range, which refers to the frequency resolution of the spectrometer being robust enough to distinguish each longitudinal mode of the light source reliably. In this particular scenario, the extent of non-ambiguity will solely be ascertained by the repetition rate of the laser.

The periodic nature of the pulse time domain in the optical frequency comb leads to

variations in the relative positions of the measured pulse and the reference pulse when there are changes in distance. This is illustrated in figure 4.7. Additionally, the measured distance also exhibits periodicity due to the peculiarities of the time domain[27].

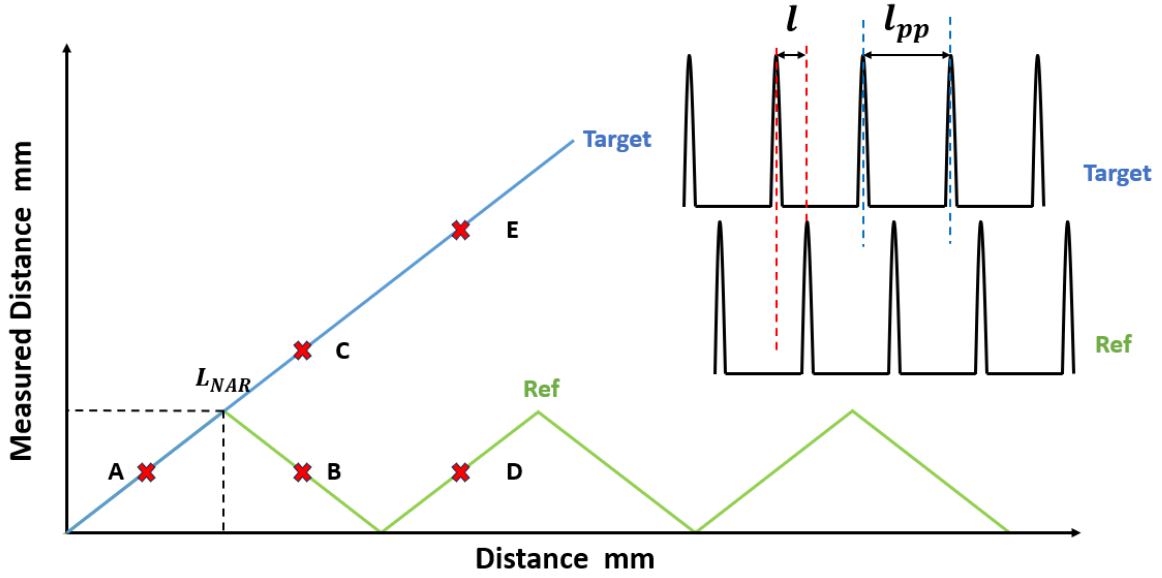


Figure 4.7: Classification of Non-ambiguity range situations

The range of relative distances between the measurement arm and the reference arm for each pulse is within the interval  $[0, \frac{L_{pp}}{2}]$ . Consequently, the maximum Non-ambiguity range for spectral interferometry may be determined by equation 4.6.

$$L_{NAR} = \frac{c}{2 \cdot f_{rep}} = \frac{L_{pp}}{2} \quad (4.6)$$

where  $L_{NAR}$  is the non-ambiguity range,  $L_{pp}$  is optical comb pulse spacing.

In this case, the non-ambiguity range can be calculated to be 7.3 mm. When the difference in optical path difference between the measurement arm and the reference arm is denoted as  $L_x \leq L_{NAR}$ , the position of the measurement point A does not experience aliasing effects. In this scenario, the first non-ambiguity range is achieved, where the measured distance and the real optical path difference are the same,  $L_{x1} = L_x$ . The actual optical path difference is  $L_x = \frac{c \cdot \tau}{2}$ ,  $\tau$  represents the time delay between the reference arm and target(measurement) arm, which is shown in the last section. In this case, the determination of the optical path difference is directly analogous to the

resolution of  $\tau$ , as previously stated in section 3.2. Figure 4.8 illustrates the optical path difference, which has been calculated by the direct evaluation of time delay, as shown in table 4.1.

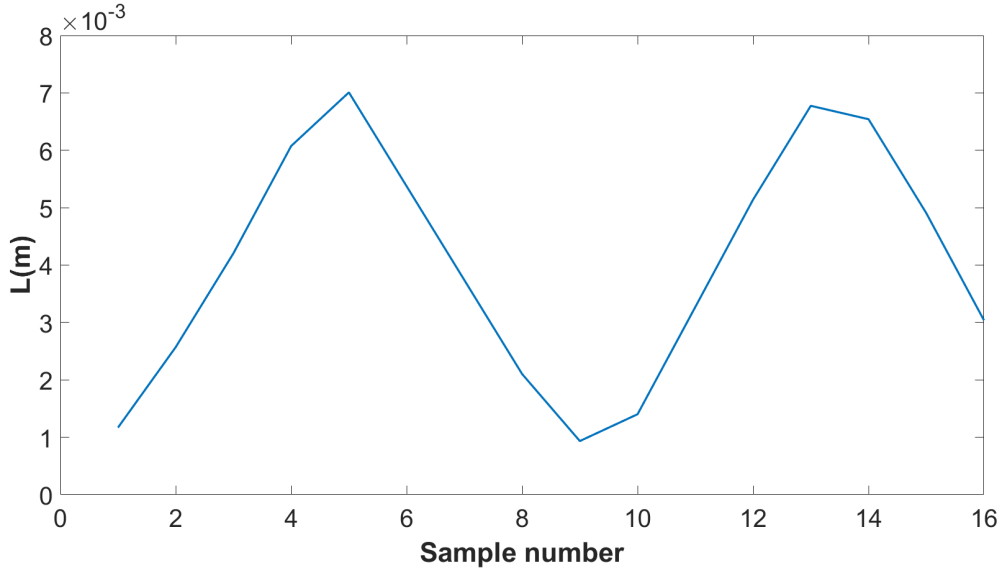


Figure 4.8: Measured distance

The aliasing effect is observed when the input signal exceeds the non-ambiguity range, which is shown in figure 4.8 and figure 4.7. The real optical path difference for points C and E in figure 4.7 may not correspond with the distance calculated based on time delay. Consequently, the equation mentioned in the preceding paragraph is only applicable when aliasing does not occur, specifically when the  $L_x \leq L_{NAR}$ . Nevertheless, the optical range difference that needs to be measured is directly linked to the preceding  $L_x$ . The occurrence of aliasing can be observed at point C. By utilizing the formula  $L_x = \frac{c\tau}{2}$ , it is possible to derive that the measured distance of point B is  $L_x$ . Point B exhibits symmetry with respect to point C about line  $L = L_{NAR}$ , the real optical distance associated with point C can be determined using equation 4.7. Similarly, point D is symmetric to point E about line  $L = 2L_{NAR}$ , and real optical distance  $L_{x3}$  can be

computed using equation 4.8.

$$L_{x2} = N \times \frac{L_{pp}}{2} + \left(\frac{L_{pp}}{2} - L_x\right) \quad (4.7)$$

$$L_{x3} = N \times \frac{L_{pp}}{2} + L_x \quad (4.8)$$

$$N = \text{round}\left(\frac{2L}{L_{pp}}\right) \quad (4.9)$$

where  $L$  represents the disparity in the optical range between the measuring arm and the reference arm. The value of  $N$  is a positive integer that is derived by rounding down the ratio of the distance to be measured to  $\frac{2L}{L_{pp}}$ .

Based on the above analysis, in cases where the measuring arm and reference arm optical path difference  $L$  is less than or equal to the non-ambiguity range  $L_{NAR}$ , the distance to be measured and the optical path difference between the measurement arm and the reference arm exhibit equivalence, thereby eliminating the occurrence of aliasing. However, as the distance measured progressively increases, the phenomenon of frequency aliasing occurs, for instance, in points C and E. The corresponding optical range difference and  $L_x$  are no longer equal. Consequently, the carrier frequency cannot be directly converted to the optical range difference that needs to be measured. Instead, its dependence is contingent upon the relative position of the pulse. Therefore, when analyzing the data, it is necessary to consider the characteristics of the trend in the carrier frequency change in order to distinguish between the two situations.

## 4.3 Discussion

The interference spectrum was obtained through experimental procedures. Subsequently, the obtained results were subjected to Fourier transform. The optical frequency comb spectra were first examined in the analysis to determine the solution for interference time delay using the peak interval method. Additionally, the maximum non-ambiguity range was analyzed and discussed in two distinct scenarios, namely case  $L_x \leq L_{NAR}$  and case  $L_x > L_{NAR}$ . The calculation of the distance to be measured was performed. The analysis of the experimental results is predicated upon measurements conducted on a singular target, specifically a single-layer case. It concurrently establishes the

groundwork for subsequent investigations involving multiple layers. When a multi-layer experiment is conducted, the target thickness can exceed the maximum non-ambiguity range. In such cases, it becomes necessary to employ the analysis method outlined in the second scenario of section 4.2.2 to accurately determine the distance to be measured.

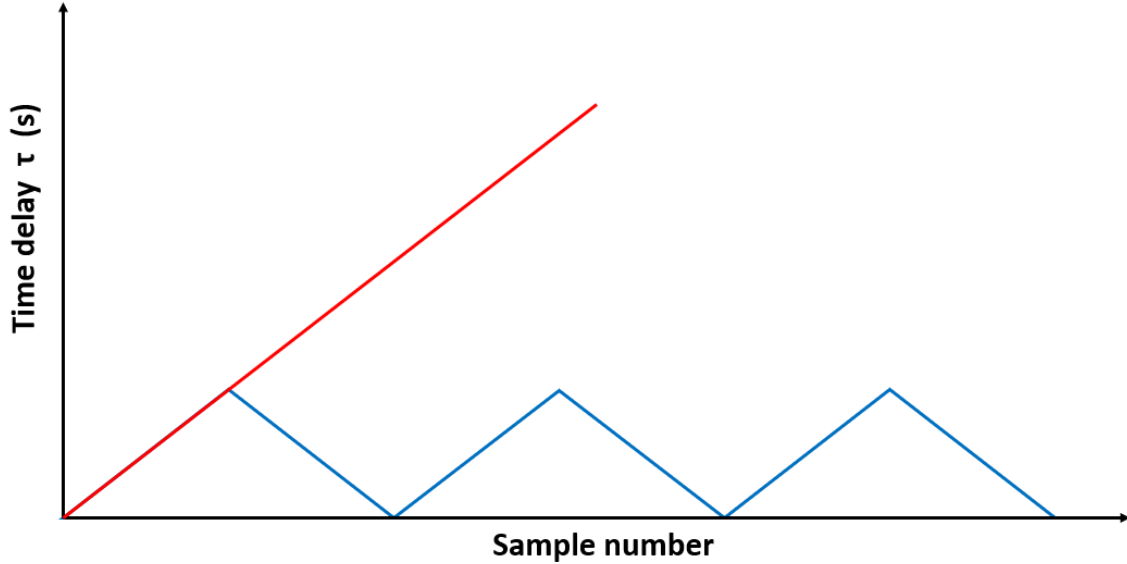


**Figure 4.9:** Classification of time delay situation

Simultaneously, the examination of the non-ambiguity range reveals a comparable association in section 4.2.1, time delay  $\tau$  is also a similar relationship. As shown in figure 4.9, the aliasing phenomenon is also observed in the time delay. This suggests that when the time delay exceeds the maximum non-ambiguity range of the time corresponding to the aliasing phenomenon will also occur. Figure 4.9 illustrates this, with the red line representing the theoretical time delay and the blue line representing the Fourier transform of the dispersive in the time delay derived from the Fourier transform of the dispersive interference signal carrier is depicted in the color blue. Moreover, the non-ambiguity range of the time delay can be calculated by the equation 4.10. The  $\tau_{NAR}$  can be seen as the maximum value of measured time delay  $\tau_{max}$ . Figure 4.10 illustrates that all  $\tau$  are smaller than  $\tau_{max}$ .

$$\tau_{NAR} = \frac{L_{NAR}}{c} = 2.44 \cdot 10^{-11} s \quad (4.10)$$

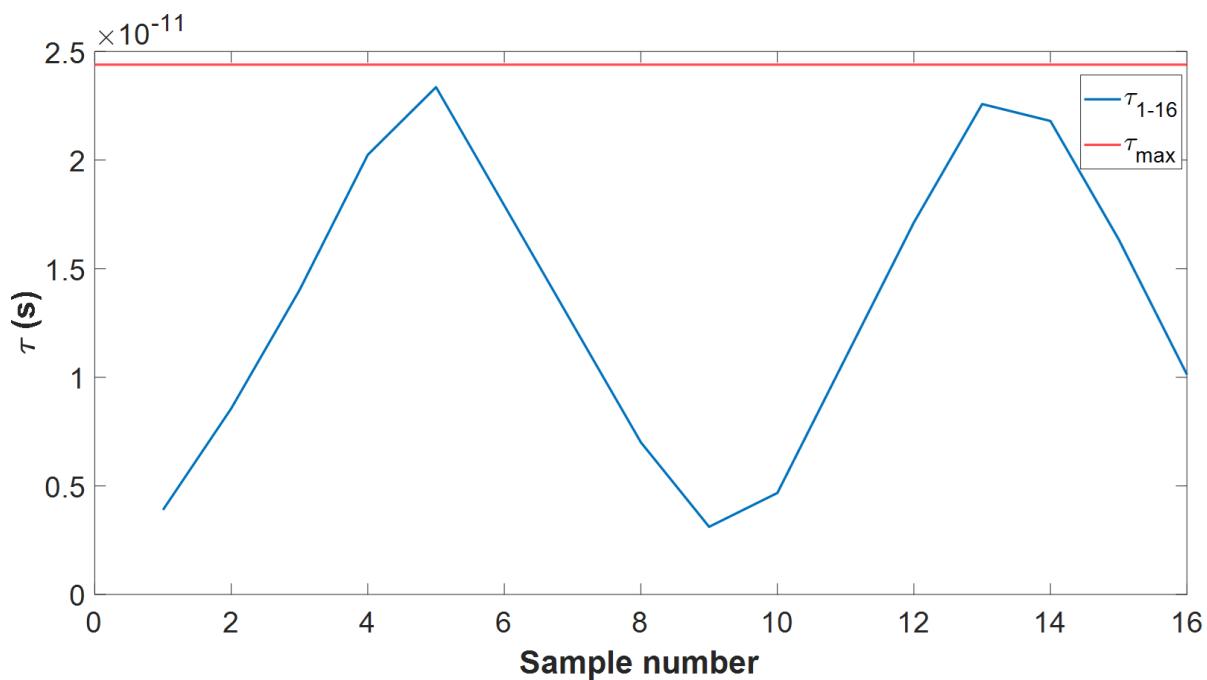


**Figure 4.10:** Temporal delay including  $\tau_{\max}$

Additionally, as shown in figure 4.8, it can be observed that the step size of the experiment is not always 1 mm. This happened because the trolley had to be moved manually in the experiment and can be improved in future experiments.

# 5

## Conclusion and Outlook

### 5.1 Conclusion

This research primarily focused on the utilization of a Mode-locked(ML) semiconductor chip laser to measure the time of flight relative to a single layer (target). Moreover, since distance and time are correlated and the calculation of time can be equated to a distance measurement. In Chapter 3, a detailed account is provided regarding the necessary types of equipment for conducting the experiment. The laser source is subjected to testing, and spectrograms are utilized to determine that the repetition frequency of the optical frequency comb aligns with the anticipated value of 20.4 GHz. The experimental setup is also provided, specifically the theoretical background, which is grounded on Michelson interference. Then the experimental procedure is given. In order to conduct a more comprehensive analysis, the experimental data (interference spectrum pattern) are subjected to a Fourier transform in Chapter 4. The peak interval approach is utilized to analyze the plots of the Fourier-transformed results in order to determine the time delay at each sampling position. The subsequent examination was an analysis of the correlation between spatial resolution and spectral bandwidth, whereby it was shown that these two variables exhibit an inverse relationship. Specifically, it was found that

as the bandwidth becomes narrower, the spatial resolution increases. The diagrams of the optical path difference between the measurement arm and the reference arm were produced directly from the time delay plots by calculation  $L_x = \frac{c\tau}{2}$ . However, there is a discrepancy between the real optical path difference and the measured distance. In this context, we present the concept of the maximum non-ambiguity range, which is established based on the spacing between optical comb pulses. The non-ambiguity range was examined and it was determined that the correlation between the difference in the optical range and the maximum non-ambiguity distance must be included during distance analysis, specifically in the context of options  $L_x \leq L_{NAR}$  and  $L_x > L_{NAR}$ . In the first scenario, where the measuring arm and reference arm optical path difference is less than or equal to the non-ambiguity range, the discrepancy between the optical range and the measured distance is equivalent. However, in the second scenario, the equivalence between the two is disrupted due to the occurrence of aliasing phenomena, necessitating another calculation method shown in section 4.2.2. Similarly, it may be inferred that the phenomena of aliasing also applies to time delays. Specifically, when the time delay exceeds the maximum non-ambiguity range corresponding to the time will also appear aliasing phenomenon.

Overall, The present experiments involving the measurement of distance (time delay) at multiple locations for a single target provide valuable insights into the potential applications of mode-locked(ML) semiconductor chip lasers in time-of-flight and distance measurements based on Michelson interferometry. Simultaneously, this establishes a foundation for subsequent assessments of targets with multi-layer.

## 5.2 Outlook

The current project investigates the time-of-flight measurements of single-layer cases. During the process of the project's experimentation phase, we encountered numerous problems that imposed limitations on the overall quality of our experimental outcomes. To enhance the procedure and experimental outcomes, different aspects might be enhanced. The following sections outline the areas that have potential for improvement.

- **Producure** : Due to software limitations, we can only move the tram manually,

which causes the step size is not always 0.1mm. In the future experiment, the step size can be modified through the utilization of an electrically controlled guide, hence enhancing the precision of the obtained outcomes.

- **Multi-layer case :** In this study, we focus on the single-layer case because of the time limitation. It can be improved for multi-layer cases. In prospective applications, the incorporation of Polydimethylsiloxane (PDMS) augmented with glass spheres can be employed as a multilayer scattering medium, which can serve as a substitute for the reflector component in this experiment. By employing an optical frequency comb light source, the interference spectrum can be obtained by implementing the Michelson Interference experiment. Subsequently, a Fourier Transform can be performed on the acquired data. The interference spectrum of each layer is subjected to Fourier transformation in order to get the respective time delay  $\tau$ , which represents the duration of photon travel through each layer. By plotting the time of flight of each layer on a single diagram, we can generate a time of flight map for this multi-layer structure. This map may then be analyzed using the algorithm described in Chapter 2 section 2.2.3 to extract the relevant optical characteristics absorption coefficient and reduced scattering coefficient, denoted as features  $\mu_a$  and  $\mu'_s$ .
- **Optical amplifier :** In this study, it has been observed that the light intensity (power) exhibits fluctuations and occasionally fails to attain the desired value. Hence, the implementation of an optical amplifier can enhance its performance.

# References

- [1] J. Sutin, B. Zimmerman, D. Tyulmankov, *et al.*, “Time-domain diffuse correlation spectroscopy”, *Optica*, vol. 3, no. 9, pp. 1006–1013, Sep. 2016. DOI: [10.1364/OPTICA.3.001006](https://doi.org/10.1364/OPTICA.3.001006). [Online]. Available: <https://opg.optica.org/optica/abstract.cfm?URI=optica-3-9-1006>.
- [2] XinHuang and JishuXian, “Application of near-infrared tissue blood oxygen parameter non-destructive monitor in the monitoring of cerebral oxygen saturation in critically ill neurosurgery patients”, *Nursing Research*, vol. 27, no. 25, pp. 2749–2751, Jan. 2013.
- [3] M. Soufineyestani, D. Dowling, and A. Khan, “Electroencephalography (eeg) technology applications and available devices”, *Applied Sciences*, vol. 10, no. 21, p. 7453, 2020.
- [4] H. Stefan and E. Trinka, “Magnetoencephalography (meg): Past, current and future perspectives for improved differentiation and treatment of epilepsies”, *Seizure*, vol. 44, pp. 121–124, 2017.
- [5] B. Rey, M. Alcañiz, J. Tembl, and V. Parkhutik, “Brain activity and presence: A preliminary study in different immersive conditions using transcranial doppler monitoring”, *Virtual Reality*, vol. 14, pp. 55–65, 2010.
- [6] A. Koht, T. B. Sloan, and J. R. Toleikis, *Monitoring the nervous system for anesthesiologists and other health care professionals*. Springer, 2012.
- [7] D. Tyulmankov, “Time-domain diffuse correlation spectroscopy: Instrument prototype, preliminary measurements, and theoretical modeling”, Ph.D. dissertation, Massachusetts Institute of Technology, 2017.

- [8] N. Coluccelli, M. Cassinero, B. Redding, H. Cao, P. Laporta, and G. Galzerano, “The optical frequency comb fibre spectrometer”, *Nature communications*, vol. 7, no. 1, pp. 1–11, 2016.
- [9] T. Fortier and E. Baumann, “20 years of developments in optical frequency comb technology and applications”, *Communications Physics*, vol. 2, no. 1, pp. 1–16, 2019.
- [10] T. Durduran, R. Choe, W. B. Baker, and A. G. Yodh, “Diffuse optics for tissue monitoring and tomography”, *Reports on progress in physics*, vol. 73, no. 7, p. 076 701, 2010.
- [11] J. A. Wahr, K. K. Tremper, S. Samra, and D. T. Delpy, “Near-infrared spectroscopy: Theory and applications”, *Journal of cardiothoracic and vascular anaesthesia*, vol. 10, no. 3, pp. 406–418, 1996.
- [12] A. Torricelli, D. Contini, A. Pifferi, *et al.*, “Time domain functional nirs imaging for human brain mapping”, *Neuroimage*, vol. 85, pp. 28–50, 2014.
- [13] H. Prabhakar, *Essentials of neuroanesthesia*. Academic Press, 2017.
- [14] O. Kholiqov, W. Zhou, T. Zhang, and V. J. Srinivasan, “Interferometric near-infrared spectroscopy (iNIRS) of human tissues in the presence of motion (Conference Presentation)”, in *Neural Imaging and Sensing 2019*, Q. Luo, J. Ding, and L. Fu, Eds., International Society for Optics and Photonics, vol. 10865, SPIE, 2019, 108650H. DOI: [10.1117/12.2507077](https://doi.org/10.1117/12.2507077). [Online]. Available: <https://doi.org/10.1117/12.2507077>.
- [15] M. S. Patterson, B. Chance, and B. C. Wilson, “Time resolved reflectance and transmittance for the noninvasive measurement of tissue optical properties”, *Applied optics*, vol. 28, no. 12, pp. 2331–2336, 1989.
- [16] M. Wolf, M. Ferrari, and V. Quaresima, “Progress of near-infrared spectroscopy and topography for brain and muscle clinical applications”, *Journal of biomedical optics*, vol. 12, no. 6, pp. 062 104–062 104, 2007.

- [17] F. Furch, T. Witting, M. Osolodkov, F. Schell, C. Schulz, and M. J. Vrakking, “High power, high repetition rate laser-based sources for attosecond science”, *Journal of Physics: Photonics*, vol. 4, no. 3, p. 032 001, 2022.
- [18] L. Chang, S. Liu, and J. E. Bowers, “Integrated optical frequency comb technologies”, *Nature Photonics*, vol. 16, no. 2, pp. 95–108, 2022.
- [19] K. Hei, G. Shi, A. Hänsel, *et al.*, “Distance metrology with integrated mode-locked ring laser”, *IEEE Photonics Journal*, vol. 11, no. 6, pp. 1–10, 2019.
- [20] N. R. Newbury, “Searching for applications with a fine-tooth comb”, *Nature photonics*, vol. 5, no. 4, pp. 186–188, 2011.
- [21] L. Wang, X. Zhao, C. Lou, *et al.*, “40gbits/s all-optical clock recovery for degraded signals using an amplified feedback laser”, *Applied Optics*, vol. 49, no. 34, pp. 6577–6581, 2010.
- [22] G.-H. Duan, A. Shen, A. Akrouf, *et al.*, “High performance inp-based quantum dash semiconductor mode-locked lasers for optical communications”, *Bell Labs Technical Journal*, vol. 14, no. 3, pp. 63–84, 2009.
- [23] J. Hazan, “Integrated widely tunable laser systems at 1300 and 1550 nm as swept sources for optical coherence tomography”, English, Proefschrift., Ph.D. dissertation, Electrical Engineering, May 2023, ISBN: 978-94-6419-804-1.
- [24] W.-C. Kuo, Y.-S. Lai, C.-M. Lai, and Y.-S. Huang, “Balanced detection spectral domain optical coherence tomography with a multiline single camera for signal-to-noise ratio enhancement”, *Applied optics*, vol. 51, no. 24, pp. 5936–5940, 2012.
- [25] H. Wu, F. Zhang, F. Meng, *et al.*, “Absolute distance measurement in a combined-dispersive interferometer using a femtosecond pulse laser”, *Measurement Science and Technology*, vol. 27, no. 1, p. 015 202, 2015.
- [26] J. Ye, “Absolute measurement of a long, arbitrary distance to less than an optical fringe”, *Optics letters*, vol. 29, no. 10, pp. 1153–1155, 2004.
- [27] K.-N. Joo and S.-W. Kim, “Absolute distance measurement by dispersive interferometry using a femtosecond pulse laser”, *Optics express*, vol. 14, no. 13, pp. 5954–5960, 2006.